J. Fluid Mech. (2023), *vol*. 967, A32, doi:10.1017/jfm.2023.513

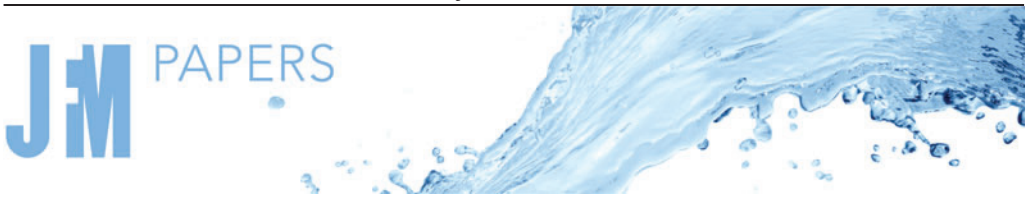

Stability of two-dimensional Taylor–Green vortices in rotating stratified fluids

Yuji Hattori[1],† **and Makoto Hirota**[1]

[1]Institute of Fluid Science, Tohoku University, Sendai 980-8577, Japan

(Received 1 April 2022; revised 13 June 2023; accepted 18 June 2023)

The linear stability of the two-dimensional Taylor–Green vortices, which is a spatially periodic array of vortices, in rotating stratified fluids is investigated by local and modal stability analysis. Five types of instability appear in general: the pure hyperbolic instability, the strato-hyperbolic instability, the rotational-hyperbolic instability, the centrifugal instability and the elliptic instability. The condition for each instability and the estimate of the growth rate, which are useful in interpreting numerical results, are obtained in the framework of local stability analysis. Realizability of an instability is introduced to predict whether an unstable mode corresponding to an unstable region found in the local stability analysis exists at finite Reynolds numbers. In the absence of stratification, the pure hyperbolic instability is dominant for weak rotation; it is stabilized for strong rotation. For strong anti-cyclonic rotation, the elliptic instability or the centrifugal instability becomes dominant depending on the parameter values; further stronger rotation stabilizes both instabilities. For strong cyclonic rotation, the rotational-hyperbolic instability or the elliptic instability becomes dominant, although the growth rate is smaller than the anti-cyclonic cases. Strong stratification changes the stability properties. The strato-hyperbolic instability occurs for weak rotation. The rotational-hyperbolic instability and the elliptic instability are weakened under cyclonic rotation, while the latter survives and extends the unstable range under anti-cyclonic rotation. The pure hyperbolic instability and the centrifugal instability are less affected by stratification. The mode structures of each instability are in good agreement with the corresponding solution to local stability equations, confirming the physical mechanism of the instability.

Key words: rotating flows, stratified flows, vortex instability

1. Introduction

Large-scale vortices are frequently encountered in the atmosphere of the earth and other planets such as Jupiter and Saturn; they also appear as coherent structures such as Gulf

† Email address for correspondence: hattori@ifs.tohoku.ac.jp

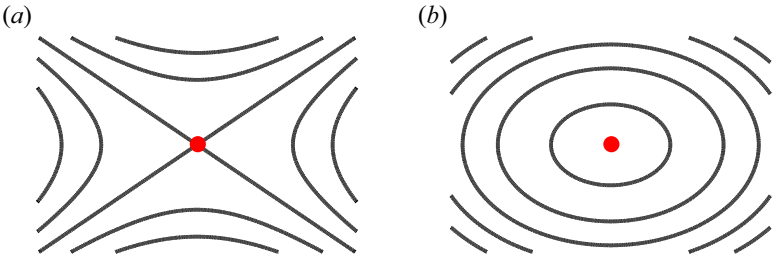

Figure 1. Steamlines near (*a*) a hyperbolic stagnation point, (*b*) an elliptic stagnation point.

Stream rings and meddies in the oceans (Thorpe 2005). The long life of the Great Red Spot on Jupiter is one of the long-standing mysteries studied by a number of researchers. These large-scale vortices in the atmosphere and the oceans sometimes form a system of vortices such as a vortex pair and an array of vortices. For example, an array of counter-rotating vortices resembling a von Kármán vortex street is often observed in the wake of an isolated island (Etling 1989; Potylitsin & Peltier 1998). On Jupiter, anti-cyclones and cyclones formed a von Kármán vortex street for approximately 50 years (Youssef & Marcus 2003). These arrays of vortices can be generated by instabilities of a jet flow and a shear flow (the Kelvin–Helmholtz instability), the baroclinic instability and other mechanisms.

The instability of the vortices on the atmosphere and the oceans is one of their most fundamental properties required for understanding their dynamics and fate. For example, most of the eddies appearing on the surface of the ocean are cyclonic, while sub-surface eddies can be anti-cyclonic (Thorpe 2005); the von Kármán vortex street in the wake of an isolated island sometimes becomes asymmetric with anti-cyclonic vortices being nearly destroyed (Potylitsin & Peltier 1998; Stegner, Pichon & Beunier 2005). The preference in the sense of rotation of the vortices is most likely caused by rotation of the system and stratification, which strongly affect the motion of the vortices in the atmosphere and the oceans. In our previous work (Hattori *et al.* 2021), the linear stability of a periodic array of vortices in non-rotating stratified fluids has been investigated in detail. The effects of rotation are studied in the present work.

Vortices in rotating stratified fluids are subject to several types of instability. The elliptic instability occurs when the streamlines near the centre of a vortex are elliptical (Miyazaki & Fukumoto 1992; Leweke & Williamson 1998; Miyazaki & Adachi 1998; Leblanc & Cambon 1998; Otheguy, Billant & Chomaz 2006*a*; Aspden & Vanneste 2009; Guimbard *et al.* 2010). The centrifugal instability appears depending on the vorticity distribution and the rate of rotation of the system (Leblanc & Cambon 1998; Potylitsin & Peltier 1998, 1999). The hyperbolic instability can occur near the hyperbolic stagnation points (Friedlander & Vishik 1991; Lifschitz & Hameiri 1991; Sipp & Jacquin 1998; Pralits, Giannetti & Brandt 2013; Suzuki, Hirota & Hattori 2018; Singh & Mathur 2019); in a two-dimensional incompressible flow, the stream function is approximated as $\Psi(x, y) = ax^2 + bxy + cy^2$ at a stagnation point $(x, y) = (0, 0)$; it is called a hyperbolic stagnation point when $b^2 - 4ac > 0$, while it is an elliptic stagnation point when $b^2 - 4ac < 0$ (figure 1). The hyperbolic instability occurs in the absence of stratification (pure hyperbolic instability), while stratification changes the resonance condition for it and the characteristics (strato-hyperbolic instability). It is particularly important for an array of vortices because the flow always possesses hyperbolic stagnation points. The zigzag instability (Billant & Chomaz 2000*a*,*b*,*c*; Otheguy, Billant & Chomaz 2006*b*; Deloncle, Billant & Chomaz 2008; Waite & Smolarkiewicz 2008; Billant 2000; Billant *et al.* 2010),

the radiative instability (Le Dizès & Billant 2009) and the transient growth (Arratia, Caulfield & Chomaz 2013; Gau & Hattori 2014) also occur in general.

How rotation and/or stratification affect the above instabilities has been studied in several previous papers. Miyazaki & Fukumoto (1992) studied the linear stability of an unbounded elliptical flow in stratified fluids, while Miyazaki (1993) extended the analysis including rotation effects. This problem was also studied by Leblanc (2003), who obtained explicit conditions for the elliptic instability by local stability analysis. The inviscid waves on a Lamb–Oseen vortex in a rotating stratified fluid were studied by Le Dizès (2008); the condition for the elliptic instability in the presence of strain was discussed, although no result for the growth rate was shown. Guimbard *et al.* (2010) investigated the effects of stratification on the elliptic instability in a rotating cylinder not only by experiments but also by theoretical analysis. The instability condition and the growth rate were shown to converge to those obtained by Leblanc (2003) in the short-wave limit. The centrifugal instability has been studied extensively since the discovery of the Rayleigh criterion (Rayleigh 1917); a criterion for rotating fluids has been derived by Kloosterziel & van Heijst (1991). Leblanc & Cambon (1998) investigated the linear stability of the Stuart vortices in rotating non-stratified fluids by modal stability analysis; the centrifugal, elliptic and pure hyperbolic instabilities were found. Sipp, Lauga & Jacquin (1999) studied the linear stability of the two-dimensional (2-D) Taylor–Green vortices in rotating non-stratified fluids by local and modal stability analysis; they also found the three instabilities reported by Leblanc & Cambon (1998). Leblanc & Godeferd (1999) showed the structures of the pure-hyperbolic-instability modes in the 2-D Taylor–Green vortices by direct numerical simulation (DNS). Potylitsin & Peltier (1998) investigated the stability of periodic vortices in rotating stratified fluids by modal stability analysis; the base flow is a quasi-steady state obtained by relaxation at low Reynolds numbers. According to them, anti-cyclonic vortices are strongly destabilized by weak rotation but stabilized by strong rotation; they also claimed that strong stratification stabilizes the vortices. These results were obtained from numerical analysis with limited resolution (the number of modes in one direction is $N_t = 37$, which is much smaller than 500 in the present work) at low Reynolds numbers ($Re = 300$). Potylitsin & Peltier (1999) investigated the stability of the Stuart vortices in rotating non-stratified fluids by modal stability analysis. Three types of instability were found: the elliptic, the centrifugal and the (pure) hyperbolic instabilities. Deloncle, Billant & Chomaz (2011) investigated the stability of vortex arrays including the von Kármán vortex street in a stratified and rotating fluid assuming that the core size of the vortices is much smaller than the distance between the vortices; the zigzag instability and the 2-D pairing instability were shown to be dominant for the 'well-separated' vortices.

Although several important aspects of the instabilities of arrays of vortices in stratified and/or rotating fluids have been elucidated, our understanding is still far from complete; there are only two papers on the arrays of vortices in rotating stratified fluids (Potylitsin & Peltier 1998; Deloncle *et al.* 2011). In particular, it is difficult to predict which instability is dominant for a given flow because the problem depends on multiple key parameters: the rotation rate of the system, the strength of stratification and the vorticity distribution, which is partially characterized by the strain rates at the stagnation points and the maximum vorticity. Moreover, the vertical scale is much smaller than the horizontal scale of the vortices in the atmosphere and the oceans; strong stratification also makes the characteristic length scale in the vertical direction small (Billant & Chomaz 2001). This implies that stability properties in a wide range of wavenumbers should be explored because the vertical wavenumber is often bounded from below because of

geometric constraint. The results obtained so far are limited to either low numerical resolution, low Reynolds numbers or a narrow range of parameter values. Thus, the stability properties of arrays of vortices in rotating stratified fluids should be further explored for a wide range of parameter values with higher resolution from a unified point of view.

In this paper, we study the linear stability of arrays of vortices in rotating stratified fluids. We clarify the condition for each instability and how the growth rate and other characteristics of the instability depend on rotation and stratification. First, we use the local stability analysis in the limit of infinite Reynolds number and large wavenumber since it is a powerful tool for parametric study; we also emphasize that it also provides physical insight into the instabilities, which is not always found by modal stability analysis. Next, the stability properties at finite Reynolds numbers and wavenumbers are obtained by modal stability analysis, where the types of modes are identified with the help of local stability results. We also show the existence of a global mode corresponding to the instability found by Sipp *et al.* (1999) and Godeferd, Cambon & Leblanc (2001) only by local stability analysis. We choose the 2-D Taylor–Green vortices as a base flow. There are several reasons for this choice: first, it is one of the few exact solutions of periodic arrays of vortices in rotating stratified fluids; second, it possesses both hyperbolic and elliptic stagnation points, which are important ingredients of arrays of vortices; third, it has been studied in previous work as a typical example of periodic arrays of vortices; and, as mentioned above, the effects of rotation on the stability of the 2-D Taylor–Green vortices have been studied by Sipp *et al.* (1999) and those of stratification have been studied in our previous work (Suzuki *et al.* 2018; Hattori *et al.* 2021). However, these two effects have not been considered simultaneously. The present work contributes to understanding the stability of vortices in rotating stratified fluids.

This paper is organized as follows. In § 2, the problem is formulated. In § 3, the instability condition and an estimate for the growth rate based on the local stability analysis are summarized; this section also includes the mechanism of the instability reported by Sipp *et al.* (1999) and Godeferd *et al.* (2001), which is named as the rotational-hyperbolic instability, and an extended analysis of the elliptic instability. The methods of the numerical stability analysis are explained in § 4. The results on the 2-D Taylor–Green vortices are presented in § 5. We conclude in § 6.

2. Problem formulation

2.1. *Governing equations*

We consider the linear stability of a periodic array of vortices to three-dimensional disturbances in stably stratified and rotating fluids. The effects of density stratification are taken into account by the Boussinesq approximation. Viscosity is taken into account, while diffusion of density is neglected since its effects are negligible (Hattori *et al.* 2021). The governing equations are

$$\boldsymbol{\nabla}\cdot\boldsymbol{u}=0, \tag{2.1}$$

$$\frac{\partial \boldsymbol{u}}{\partial t}+\boldsymbol{u}\cdot\boldsymbol{\nabla}\boldsymbol{u}+2\Omega_0\boldsymbol{e}_z\times\boldsymbol{u}=-\frac{1}{\rho_0}\boldsymbol{\nabla}p-g\frac{\rho}{\rho_0}\boldsymbol{e}_z+\nu\Delta\boldsymbol{u}, \tag{2.2}$$

$$\frac{\partial \rho}{\partial t}+\boldsymbol{u}\cdot\boldsymbol{\nabla}\rho=0, \tag{2.3}$$

where $\boldsymbol{u}$, p and ρ are the velocity, pressure and density fields, respectively, Ω_0 is the angular velocity, ρ_0 is a constant reference density, g is the acceleration of gravity and ν is

the kinematic viscosity. We consider high-Reynolds-number flows throughout the paper; in the local stability analysis, we neglect viscous diffusion, while the Reynolds number is set to $Re = 10^5$ in the modal stability analysis.

We consider a 2-D base flow. The vorticity equation for 2-D flows in a rotating frame under the Boussinesq approximation reads

$$\frac{\partial \omega_z}{\partial t} + \frac{\partial \Psi}{\partial y}\frac{\partial(\omega_z + 2\Omega_0)}{\partial x} - \frac{\partial \Psi}{\partial x}\frac{\partial(\omega_z + 2\Omega_0)}{\partial y} = \nu \Delta \omega_z, \tag{2.4}$$

where $\Psi = -\Delta^{-1}\omega_z$ is the stream function of the base flow. Since Ω_0 is constant, any 2-D flow that satisfies

$$\frac{\partial \Psi}{\partial y}\frac{\partial \omega_z}{\partial x} - \frac{\partial \Psi}{\partial x}\frac{\partial \omega_z}{\partial y} = 0 \tag{2.5}$$

is steady in the absence of viscous diffusion. Equation (2.5) is the well-known condition for 2-D steady inviscid flows without rotation and stratification. In other words, rotation and stratification do not affect the condition for steadiness under the Boussinesq approximation and uniform rotation.

The base flow is assumed steady not only in local stability analysis but also in modal stability analysis because the growth of instabilities is much faster than the time evolution of the base flow due to viscous diffusion at $Re = 10^5$. The velocity, pressure and density fields are decomposed as

$$\boldsymbol{u} = \boldsymbol{u}_b + \boldsymbol{u}', \tag{2.6}$$

$$p = p_b + p', \tag{2.7}$$

$$\rho = \rho_0 + \alpha z + \rho', \tag{2.8}$$

where $(\boldsymbol{u}_b, p_b, \rho_b)$ and $(\boldsymbol{u}', p', \rho') = (u_x', u_y', u_z', p', \rho')$ are the base flow and the disturbance, the direction of the gravity force is taken as $-\boldsymbol{e}_z$ and the base density is assumed to be $\rho_b = \rho_0 + \alpha z$ with $\alpha = \partial \rho_b / \partial z < 0$ being a constant. The magnitude of the disturbance is infinitesimally small. Then the governing equations of the disturbance in non-dimensionalized form are

$$\boldsymbol{\nabla} \cdot \boldsymbol{u}' = 0, \tag{2.9}$$

$$\frac{\partial \boldsymbol{u}'}{\partial t} + (\boldsymbol{u}' \cdot \boldsymbol{\nabla})\boldsymbol{u}_b + (\boldsymbol{u}_b \cdot \boldsymbol{\nabla})\boldsymbol{u}' + \frac{1}{Ro}\boldsymbol{e}_z \times \boldsymbol{u}' = -\boldsymbol{\nabla} p' - \rho' \boldsymbol{e}_z + \frac{1}{Re}\nabla^2 \boldsymbol{u}', \tag{2.10}$$

$$\frac{\partial \rho'}{\partial t} + (\boldsymbol{u}_b \cdot \boldsymbol{\nabla})\rho' - \frac{1}{F_h^2} u_z' = 0, \tag{2.11}$$

where $Ro = U_0/(2\Omega_0 L_0)$ is the Rossby number, $Re = U_0 L_0/\nu$ is the Reynolds number, $F_h = U_0/(L_0 N)$ is the Froude number based on the horizontal scale, $N = \sqrt{-\alpha g/\rho_0}$ is the Brunt–Väisälä frequency, and U_0 and L_0 are a characteristic velocity and a length scale, respectively; see § 4 for the actual choice of U_0 and L_0. In the following, the values are scaled by U_0 and L_0 unless stated explicitly.

In the local stability analysis, the disturbance is assumed to be in the form of a wave packet with short wavelength:

$$\boldsymbol{u}' = \left(\hat{\boldsymbol{u}}_0 + \delta\hat{\boldsymbol{u}}_1 + \cdots\right)\exp\left(\frac{\mathrm{i}}{\delta}\Phi\right), \tag{2.12}$$

$$p' = \left(\hat{p}_0 + \delta\hat{p}_1 + \cdots\right)\exp\left(\frac{\mathrm{i}}{\delta}\Phi\right), \tag{2.13}$$

$$\rho' = \left(\hat{\rho}_0 + \delta\hat{\rho}_1 + \cdots\right)\exp\left(\frac{\mathrm{i}}{\delta}\Phi\right), \tag{2.14}$$

where δ is a small parameter proportional to the wavelength and Φ is eikonal which is assumed to satisfy $D\Phi/Dt = 0$ ($D/Dt = \partial/\partial t + \boldsymbol{u}_b \cdot \boldsymbol{\nabla}$). Viscosity is neglected in the local stability analysis. Substituting the above expressions into (2.9)–(2.11) yields a set of ordinary differential equations at the leading order:

$$\frac{\mathrm{d}\boldsymbol{X}}{\mathrm{d}t} = \boldsymbol{U}(\boldsymbol{X}), \tag{2.15}$$

$$\frac{\mathrm{d}\boldsymbol{k}}{\mathrm{d}t} = -\boldsymbol{L}^{\mathrm{T}}\boldsymbol{k}, \tag{2.16}$$

$$\frac{\mathrm{d}\boldsymbol{a}}{\mathrm{d}t} = (2\hat{\boldsymbol{k}}\hat{\boldsymbol{k}}^{\mathrm{T}} - \boldsymbol{I})\boldsymbol{L}\boldsymbol{a} + (\hat{\boldsymbol{k}}\hat{\boldsymbol{k}}^{\mathrm{T}} - \boldsymbol{I})r\boldsymbol{e}_z + \frac{1}{Ro}(\hat{\boldsymbol{k}}\hat{\boldsymbol{k}}^{\mathrm{T}} - \boldsymbol{I})\boldsymbol{e}_z \times \boldsymbol{a}, \tag{2.17}$$

$$\frac{\mathrm{d}r}{\mathrm{d}t} = \frac{1}{F_h^2}a_z, \tag{2.18}$$

where $\boldsymbol{L}_{ij} = \partial U_i/\partial x_j$ and $\hat{\boldsymbol{k}} = \boldsymbol{k}/|\boldsymbol{k}|$ (Friedlander & Vishik 1991; Lifschitz & Hameiri 1991; Leblanc 1997). Here, $\boldsymbol{X}$ is the position of the fluid particle and $\boldsymbol{k} = \boldsymbol{\nabla}\Phi$ is the local wavevector, while $\boldsymbol{a} = \hat{\boldsymbol{u}}_0$ and $r = \hat{\rho}_0$ are the amplitudes of the disturbance corresponding to velocity and density, respectively. The incompressibility condition in (2.9) leads to $\boldsymbol{a} \cdot \boldsymbol{k} = 0$, which is satisfied for $t > 0$ if it holds at $t = 0$. The base flow is unstable if the amplitude $\{\boldsymbol{a}, r\}$ grows without bound.

2.2. *Useful equations and approximations*

Before showing the condition for each instability and the estimate of the growth rate, useful equations and approximations are presented. We are left with four (2.17) and (2.18) after solving (2.15) and (2.16). The incompressibility condition $\boldsymbol{a} \cdot \boldsymbol{k} = 0$ implies that the actual degree of freedom is three; it is further reduced to two using conservation of potential vorticity (Aspden & Vanneste 2009; Suzuki *et al.* 2018).

First, we introduce

$$p = \frac{k}{|\boldsymbol{k}_\perp|}\boldsymbol{k}_\perp \cdot \boldsymbol{a}_\perp = -\frac{kk_z}{|\boldsymbol{k}_\perp|}a_z, \quad q = \left(\frac{k}{|\boldsymbol{k}_\perp|}\boldsymbol{k}_\perp \times \boldsymbol{a}_\perp\right) \cdot \boldsymbol{e}_z, \quad s = \frac{k}{|\boldsymbol{k}_\perp|}r \tag{2.19a–c}$$

as done by Bayly, Holm & Lifschitz (1996), where $\boldsymbol{k}_\perp = (k_x, k_y)^{\mathrm{T}}$ and $\boldsymbol{a}_\perp = (a_x, a_y)^{\mathrm{T}}$ are the horizontal projections of $\boldsymbol{k}$ and $\boldsymbol{a}$, respectively. Then, (2.17) and (2.18) reduce to

$$\frac{\mathrm{d}}{\mathrm{d}t}\begin{pmatrix} p \\ q \\ s \end{pmatrix} = \begin{pmatrix} \dfrac{\mathrm{d}}{\mathrm{d}t}\log\dfrac{|\boldsymbol{k}_\perp|}{|\boldsymbol{k}|} & \dfrac{2k_z^2\boldsymbol{H}\boldsymbol{k}_\perp\cdot\boldsymbol{k}_\perp}{|\boldsymbol{k}|^2|\boldsymbol{k}_\perp|^2} + \dfrac{k_z^2}{Rok^2} & \dfrac{|\boldsymbol{k}_\perp|^2}{|\boldsymbol{k}|^2}k_z \\ -\omega_z - Ro^{-1} & -\dfrac{\mathrm{d}}{\mathrm{d}t}\log\dfrac{|\boldsymbol{k}_\perp|}{|\boldsymbol{k}|} & 0 \\ -\dfrac{1}{F_h^2 k_z} & 0 & -\dfrac{\mathrm{d}}{\mathrm{d}t}\log\dfrac{|\boldsymbol{k}_\perp|}{|\boldsymbol{k}|} \end{pmatrix}\begin{pmatrix} p \\ q \\ s \end{pmatrix}, \tag{2.20}$$

where

$$\boldsymbol{L} = \begin{pmatrix} \boldsymbol{L}_\perp & 0 \\ 0 & 0 \end{pmatrix}, \quad \boldsymbol{H} = \boldsymbol{L}_\perp\begin{pmatrix} 0 & 1 \\ -1 & 0 \end{pmatrix}. \tag{2.21a,b}$$

By eliminating p from the equations for p and q, we have

$$\frac{\mathrm{d}^2 q}{\mathrm{d}t^2} = U_q q + D_s s, \tag{2.22}$$

where

$$U_q = \left(\frac{\mathrm{d}}{\mathrm{d}t}\log\frac{|\boldsymbol{k}_\perp|}{|\boldsymbol{k}|}\right)^2 - \frac{\mathrm{d}^2}{\mathrm{d}t^2}\log\frac{|\boldsymbol{k}_\perp|}{|\boldsymbol{k}|} - \left(\frac{2k_z^2\boldsymbol{H}\boldsymbol{k}_\perp\cdot\boldsymbol{k}_\perp}{|\boldsymbol{k}|^2|\boldsymbol{k}_\perp|^2} + \frac{k_z^2}{Rok^2}\right)(\omega_z + Ro^{-1}), \tag{2.23}$$

$$D_s = -\frac{|\boldsymbol{k}_\perp|^2}{|\boldsymbol{k}|^2}k_z(\omega_z + Ro^{-1}). \tag{2.24}$$

We can also eliminate p from the equations for q and s, which leads to

$$\frac{\mathrm{d}q}{\mathrm{d}t} - F_h^2(\omega_z + Ro^{-1})k_z\frac{\mathrm{d}s}{\mathrm{d}t} = -\left(\frac{\mathrm{d}}{\mathrm{d}t}\log\frac{|\boldsymbol{k}_\perp|}{|\boldsymbol{k}|}\right)(q - F_h^2(\omega_z + Ro^{-1})k_z s). \tag{2.25}$$

Since ω_z and k_z are constant along a streamline, we have

$$\frac{\mathrm{d}}{\mathrm{d}t}\left[\left(\frac{|\boldsymbol{k}_\perp|}{|\boldsymbol{k}|}\right)(q - F_h^2(\omega_z + Ro^{-1})k_z s)\right] = 0 \tag{2.26}$$

or

$$q - F_h^2(\omega_z + Ro^{-1})k_z s = C_{pv}\frac{|\boldsymbol{k}|}{|\boldsymbol{k}_\perp|}, \tag{2.27}$$

where C_{pv} is a constant. For an unstable solution which grows exponentially, the right-hand side of (2.27) can be neglected so that we have

$$q = F_h^2(\omega_z + Ro^{-1})k_z s. \tag{2.28}$$

Then the equation for q becomes a closed equation

$$\frac{\mathrm{d}^2 q}{\mathrm{d}t^2} = V_q q, \tag{2.29}$$

Type of instability	Condition	Growth rate
Pure hyperbolic (PH)	$\lvert Ro^{-1}\rvert < \varepsilon_h$	$C_{PH}(\varepsilon_h^2 - Ro^{-2})^{1/2}$
Strato-hyperbolic (SH)	$\lvert Ro^{-1}\rvert < \varepsilon_h, F_h^{-1} \gtrsim \omega_{max}/2$	$C_{SH}(\varepsilon_h^2 - Ro^{-2})^{1/2}$
Rotational-hyperbolic (RH)	$\lvert Ro^{-1}\rvert \gtrsim \varepsilon_h$	$C_{RH}\varepsilon_h$
Centrifugal (C)	$-\omega_{max} < Ro^{-1} < 0$	$C_C\omega_{max}$
Elliptic (E)	$F_h^{-1} < \frac{1}{2}\omega_{max}, Ro^{-1} < -\frac{3}{2}\omega_{max}$ or $Ro^{-1} > -\frac{1}{2}\omega_{max}$	$C_E\varepsilon_e$
	$F_h^{-1} > \frac{1}{2}\omega_{max}, -\frac{3}{2}\omega_{max} < Ro^{-1} \lesssim 0$	$C_E\varepsilon_e$

Table 1. Condition and growth rate estimated by local stability analysis. The C_{PH}, C_{SH}, C_{RH}, C_C and C_E are $O(1)$ coefficients which depend on the parameters in general.

Case	ε_h	ε_e	ω_{max}
$\varepsilon_e/\omega_{max} = 0$	3.14	0	6.28
$\varepsilon_e/\omega_{max} = 0.2$	2.88	1.26	6.28

Table 2. Strain rates at hyperbolic and elliptic stagnation points and maximum vorticity of 2-D Taylor–Green vortices considered in the present paper.

where

$$V_q = \left(\frac{\mathrm{d}}{\mathrm{d}t}\log\sin\theta\right)^2 - \frac{\mathrm{d}^2}{\mathrm{d}t^2}\log\sin\theta - (2\boldsymbol{H}\hat{\boldsymbol{k}}_\perp\cdot\hat{\boldsymbol{k}}_\perp\cos^2\theta + Ro^{-1}\cos^2\theta)(\omega_z + Ro^{-1}) - F_h^{-2}\sin^2\theta, \tag{2.30}$$

and $\theta = \cos^{-1} k_z/|\boldsymbol{k}|$ is the angle of wavevector and $\hat{\boldsymbol{k}}_\perp = \boldsymbol{k}_\perp/|\boldsymbol{k}_\perp|$. We use (2.29) in some of the following subsections.

3. Instability condition and estimate of growth rates

In this section, we consider the condition for each instability and estimate the growth rate in the framework of local stability analysis; most of them have been already obtained in previous work, although there are new results for the rotational-hyperbolic instability and the elliptic instability. Our aim is to give concise and useful expressions of the instability condition and the growth rate for each instability under the common scaling, which are not always rigorous but allow us to compare between the instabilities and to interpret the results in § 5 without difficulties. They are summarized in table 1, which are applicable to any flow if the actual values of the strain rates ε_h and ε_e at the hyperbolic and elliptic stagnation points, respectively, and the maximum vorticity ω_{max} are available (see table 2 in § 4 for the 2-D Taylor–Green vortices); here, the strain rate is the larger eigenvalue of the 2×2 matrix (or the strain tensor) $(\boldsymbol{L}_\perp + \boldsymbol{L}_\perp^{\mathrm{T}})/2$; note that the sum of the eigenvalues are zero for incompressible flows. It is pointed out that the most essential dependence on the parameters is shown for the growth rate in table 1. Note that the $O(1)$ coefficients C_{PH}, C_{SH}, C_{RH}, C_C and C_E in table 1 depend on the parameters in general; the actual

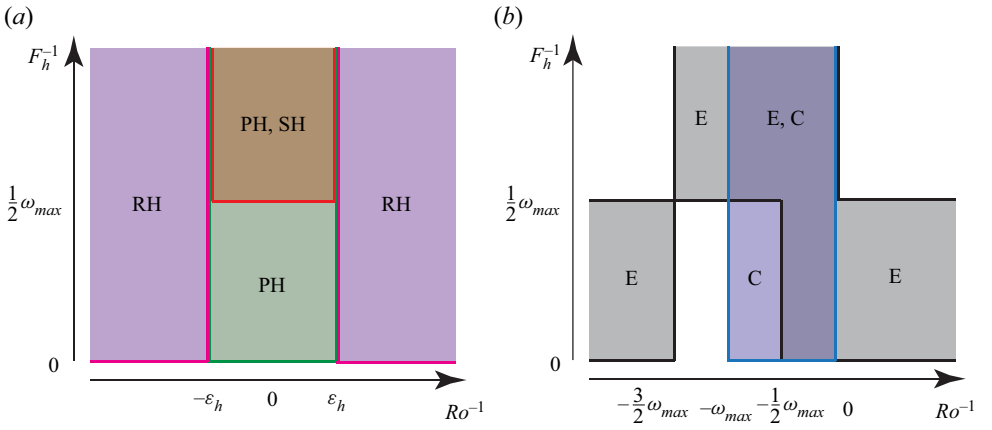

Figure 2. Unstable regions on (Ro^{-1}, F_h^{-1}) plane estimated by local stability analysis. (*a*) Pure hyperbolic, strato-hyperbolic and rotational-hyperbolic instabilities, (*b*) centrifugal and elliptic instabilities.

dependence will be checked numerically in § 5.1 (figure 8). The instability conditions are visualized on the (Ro^{-1}, F_h^{-1}) plane in figure 2.

3.1. *Pure hyperbolic instability*

The pure hyperbolic (PH) instability is due to stretching near the hyperbolic stagnation points (Friedlander & Vishik 1991; Lifschitz & Hameiri 1991; Leblanc 1997). The mechanism and the growth rate can be estimated analytically by investigating the solution to (2.17) at the hyperbolic stagnation points. We set $\theta = 0^\circ$ or $\boldsymbol{k}_\perp = 0$ for which the growth rate is maximum and stratification has no effect as will be confirmed in § 5. Then the equation for $\boldsymbol{a}_\perp$ reads

$$\frac{\mathrm{d}\boldsymbol{a}_\perp}{\mathrm{d}t} = \begin{pmatrix} -\dfrac{\partial u_b}{\partial x} & -\dfrac{\partial u_b}{\partial y} + Ro^{-1} \\ -\dfrac{\partial v_b}{\partial x} - Ro^{-1} & -\dfrac{\partial v_b}{\partial y} \end{pmatrix} \begin{pmatrix} a_x \\ a_y \end{pmatrix}. \tag{3.1}$$

Let us consider a hyperbolic stagnation point where the flow is expanded as $(u_b, v_b) = \varepsilon_h(x, -y) + O(x^2 + y^2)$. Then the above equation becomes

$$\frac{\mathrm{d}\boldsymbol{a}_\perp}{\mathrm{d}t} = \begin{pmatrix} -\varepsilon_h & Ro^{-1} \\ -Ro^{-1} & \varepsilon_h \end{pmatrix} \begin{pmatrix} a_x \\ a_y \end{pmatrix}, \tag{3.2}$$

where $\varepsilon_h = \partial u_b/\partial x = -(\partial v_b/\partial y)$ is the strain rate. The eigenvalues of the matrix in (3.2) are given by

$$\lambda^2 = \varepsilon_h^2 - Ro^{-2}. \tag{3.3}$$

Thus, the pure hyperbolic instability occurs when $|Ro^{-1}| < \varepsilon_h$. The above (3.2) has a simple solution:

$$a_x = a_x(0)\mathrm{e}^{-\varepsilon_h t}, \quad a_y = a_y(0)\mathrm{e}^{\varepsilon_h t}, \tag{3.4a,b}$$

when $Ro^{-1} = 0$ (Friedlander & Vishik 1991; Lifschitz & Hameiri 1991). In this regard, a_y is in the stretching phase, while a_x is in the compression phase. However, when the fluid particle is away from the hyperbolic stagnation points so that the strain rate is small, the

phase of $\boldsymbol{a}$ changes approximately as $\boldsymbol{a} \propto \mathrm{e}^{\pm \mathrm{i} Ro^{-1} t}$, which we call the oscillation phase below.

In general, an estimate for the growth rate on a closed streamline is required. In this case, we should take into account that the wave packet does not always grow with the eigenvalue λ; it is either stretched or compressed near the hyperbolic stagnation points depending on the direction of $\boldsymbol{a}$; when it is away from the hyperbolic stagnation points, the direction of $\boldsymbol{a}$ rotates in the oscillation phase. Therefore, the growth rate is estimated as $\sigma = C_{PH}(\varepsilon_h^2 - Ro^{-2})^{1/2}$, where $C_{PH} \lesssim 1$ is a coefficient determined by the ratio of time of the stretching phase, in which the fluid particle stays near the stagnation points, and the oscillation phase, in which the fluid particle travels between the stagnation points. In the short-wave limit, the instability condition and the growth rate are unaffected by stratification because it occurs for $\theta = 0^\circ$ where the stratification effects vanish.

3.2. *Strato-hyperbolic instability*

The strato-hyperbolic (SH) instability is a variant of the pure hyperbolic instability under stratification effects; it occurs when the exponential growth near the hyperbolic stagnation points is connected with phase shift due to the gravity waves in favour of exponential growth. Although the waves become inertia-gravity waves under rotation effects, the condition and the growth rate are estimated similarly as for the pure hyperbolic instability; the growth rate is estimated as $\sigma = C_{SH}(\varepsilon_h^2 - Ro^{-2})^{1/2}$; it is stabilized when $|Ro^{-1}| > \varepsilon_h$. The coefficient C_{SH} is smaller than C_{PH} in general because the ratio of the stretching phase to the oscillation phase decreases for larger θ, where the strato-hyperbolic instability occurs. One important difference, however, is that the frequency of the gravity wave should be large enough to generate the phase shift during the fluid particle motion where the frequency is approximated as $\omega_{max}/2$; this leads to $F_h^{-1} \gtrsim \omega_{max}/2$ as an instability condition (Suzuki *et al.* 2018). The resonance condition for the instability derived by Suzuki *et al.* (2018) can be generalized as

$$\int_0^{T/2} \sqrt{Ro^{-2}\cos^2\theta + F_h^{-2}\sin^2\theta}\,\mathrm{d}t = m\pi, \tag{3.5}$$

where T is the period of fluid particle motion and m is a positive integer. When F_h^{-1} is large, the left-hand side of the above equation increases monotonically with θ_0, so that the resonance condition is satisfied for $|Ro^{-1}| \lesssim 2m\pi/T \lesssim F_h^{-1}$; thus, the strato-hyperbolic instability exists in the limit of strong stratification.

3.3. *Rotational-hyperbolic instability*

Although the pure hyperbolic instability is stabilized for $|Ro^{-1}| > \varepsilon_h$, the potential V_q in (2.29) oscillates periodically along streamlines near the cell boundaries. In fact, V_q is approximated as

$$V_q \approx -\frac{\mathrm{d}^2}{\mathrm{d}t^2}\log\sin\theta - Ro^{-2}\cos^2\theta - F_h^{-2}\sin^2\theta \tag{3.6}$$

near the cell boundaries; the first term is the main source of oscillation, while the other terms are responsible for the inertia-gravity waves. This oscillation can resonate with the inertia-gravity waves to give rise to another instability; we call it rotational-hyperbolic (RH) instability because it is the motion near the hyperbolic points which is responsible

for the oscillation of V_q. This instability has been shown by Sipp *et al.* (1999) without much attention and found by Godeferd *et al.* (2001) both by local stability analysis, while its nature should be further explored because the corresponding unstable mode has not been found in modal stability analysis. Since the time period of the fluid particle motion is large on streamlines near the cell boundaries, the resonance occurs for small frequency of the inertia-gravity waves: $\theta \approx \pi/2$ and small F_h^{-1}. The growth rate is estimated as $\sigma = C_{RH}\varepsilon_h$, where C_{RH} is in general smaller than C_{PH} since the wavevector angle θ is larger than the pure hyperbolic instability. The resonance condition for the rotational-hyperbolic instability is the same as (3.5) for the strato-hyperbolic instability; since it is satisfied for $\min(|Ro^{-1}|, F_h^{-1}) \lesssim 2m\pi/T \lesssim \max(|Ro^{-1}|, F_h^{-1})$, the rotational-hyperbolic instability exists in the limit of strong stratification or rotation, although the growth rate becomes small for higher resonance (large m).

3.4. *Centrifugal instability*

The centrifugal (C) instability has been studied extensively since the discovery of the Rayleigh criterion (Rayleigh 1917); a criterion for rotating fluids was derived by Kloosterziel & van Heijst (1991). We set $\theta = 0^\circ$ or $\boldsymbol{k}_\perp = 0$ where the growth rate is maximum and stratification has no effect. In addition, we approximate the base flow by an axisymmetric flow

$$\boldsymbol{U} = U_\Theta^{(0)}(R)\boldsymbol{e}_\Theta \tag{3.7}$$

in the polar coordinates (R, Θ) centred at an elliptic stagnation point to obtain concise expressions for the instability condition and growth rate. Then the equation for $\boldsymbol{a}_\perp = a_R\boldsymbol{e}_R + a_\Theta\boldsymbol{e}_\Theta$ reads

$$\frac{\mathrm{d}}{\mathrm{d}t}\begin{pmatrix} a_R \\ a_\Theta \end{pmatrix} + \Omega_p \begin{pmatrix} -a_\Theta \\ a_R \end{pmatrix} = \begin{pmatrix} 0 & \Omega_p + Ro^{-1} \\ -\dfrac{\mathrm{d}U_\Theta^{(0)}}{\mathrm{d}R} - Ro^{-1} & 0 \end{pmatrix} \begin{pmatrix} a_R \\ a_\Theta \end{pmatrix}, \tag{3.8}$$

where $\Omega_p = U_\Theta^{(0)}/R$ is the rotation rate of a fluid particle. The above equation is reduced to

$$\frac{\mathrm{d}^2 a_R}{\mathrm{d}t^2} = -2\left(\Omega_p + \frac{Ro^{-1}}{2}\right)(\omega_z + Ro^{-1})a_R, \tag{3.9}$$

where $\omega_z = \mathrm{d}U_\Theta^{(0)}/\mathrm{d}R + U_\Theta^{(0)}/R$ is the vorticity. Thus, the Rayleigh criterion in rotating fluids is recovered as the condition for the centrifugal instability:

$$\left(\Omega_p + \frac{Ro^{-1}}{2}\right)(\omega_z + Ro^{-1}) < 0 \tag{3.10}$$

or

$$-2\Omega_p < Ro^{-1} < -\omega_z \tag{3.11}$$

on each streamline. We assume that ω_z decreases monotonically with R and $\omega_z \geq 0$. Then, Ω_p is maximum at $R = 0$ where $2\Omega_p = \omega_z(0) = \omega_{max}$, by which the instability condition

becomes

$$-\omega_{max} < Ro^{-1} < 0. \tag{3.12}$$

The maximum growth rate depends on the vorticity distribution. The growth rate at a given streamline takes the maximum value when $-Ro^{-1} = \Omega_p(R) + \omega_z(R)/2$:

$$\sigma = \Omega_p - \frac{\omega_z}{2} = C_C \omega_{max}, \tag{3.13}$$

where C_C is an $O(1)$ coefficient.

3.5. *Elliptic instability*

The elliptic (E) instability in rotating stratified fluids was studied by Kerswell (2002) and Leblanc (2003) for the unbounded case, and by Guimbard *et al.* (2010) for the flow inside a rotating cylinder; see also Godeferd *et al.* (2001) for the rotating non-stratified case and Miyazaki & Fukumoto (1992) for the non-rotating stratified case. Here we derive a new result required for interpretation of the results in § 5 after recovering the results obtained by Kerswell (2002) and Leblanc (2003).

We assume that the base flow is a sum of an axisymmetric flow and a weak straining flow:

$$\boldsymbol{U} = U_\Theta^{(0)}(R)\boldsymbol{e}_\Theta + \varepsilon_e \left[U_R^{(1)}(R) \sin 2\Theta \boldsymbol{e}_r + U_\Theta^{(1)}(R) \cos 2\Theta \boldsymbol{e}_\Theta \right]. \tag{3.14}$$

The potential in (2.29) turns out to be

$$V_q = V_q^{(0)} + \varepsilon_e V_q^{(1)} \cos 2\Omega_p t + O(\varepsilon_e^2), \tag{3.15}$$

$$V_q^{(0)} = -(2\Omega_p + Ro^{-1})(\omega_z + Ro^{-1}) \cos^2\theta - F_h^{-2} \sin^2\theta, \tag{3.16}$$

$$\begin{aligned} V_q^{(1)} = {} & 2\Omega_p \cos^2\theta \left(\frac{U_R^{(1)}}{R_0} + \frac{\mathrm{d}U_R^{(1)}}{\mathrm{d}R} - \frac{U_R^{(1)}}{R_0\Omega_p} \frac{\mathrm{d}U_\Theta^{(0)}}{\mathrm{d}R} \right) - 2\cos^2\theta(\omega_z + Ro^{-1}) \\ & + \left[-\gamma \sin^2\theta \frac{\mathrm{d}U_R^{(1)}}{\mathrm{d}R} - \left(\frac{3}{2} + \gamma \sin^2\theta \right) \frac{U_R^{(1)}}{R_0} \right. \\ & \left. + \frac{U_\Theta^{(1)}}{R_0} + \left(-\frac{1}{2} + \gamma \sin^2\theta \right) \frac{U_R^{(1)}}{R_0\Omega_p} \frac{\mathrm{d}U_\Theta^{(0)}}{\mathrm{d}R} \right] \\ & - \frac{\sin^2\theta \cos^2\theta}{F_h^2 \Omega_p} \left(\frac{U_R^{(1)}}{R_0} + \frac{\mathrm{d}U_R^{(1)}}{\mathrm{d}R} - \frac{U_R^{(1)}}{R_0\Omega_p} \frac{\mathrm{d}U_\Theta^{(0)}}{\mathrm{d}R} \right), \end{aligned} \tag{3.17}$$

where $\gamma = 1 + 1/(2Ro\Omega_p)$. The leading-order term determines the oscillation frequency ω by $\omega^2 = -V_q^{(0)}$, while the first-order term can induce resonance so that an instability occurs.

First, we focus on the stability near the elliptic stagnation points. At $R \approx 0$, $\omega_z \approx 2\Omega_p \approx \omega_{max}$, which gives

$$\omega^2 = -V_q^{(0)} \approx (\omega_{max} + Ro^{-1})^2 \cos^2\theta + F_h^{-2} \sin^2\theta. \tag{3.18}$$

The resonance condition is

$$\omega = \frac{n}{2}\omega_{max}, \tag{3.19}$$

which gives, for $n = 1$,

$$\cos^2\theta = \frac{1}{4}\frac{\omega_{max}^2 - 4F_h^{-2}}{(\omega_{max} + Ro^{-1})^2 - F_h^{-2}}. \tag{3.20}$$

When (3.20) has a solution, the growth rate is obtained as

$$\sigma = \frac{\varepsilon_e}{64}\left|\frac{(\omega_{max}^2 - 4F_h^{-2})\left(3\omega_{max} + 2Ro^{-1}\right)^2}{\left[(\omega_{max} + Ro^{-1})^2 - F_h^{-2}\right]\omega_{max}^2}\right|, \tag{3.21}$$

which recovers the result by Leblanc (2003) with $\omega_{max} = 2, Ro^{-1} = 2f, F_h^{-1} = 2n$ and $\varepsilon = \delta/2$. The instability condition is obtained by considering $0 \le \cos^2\theta \le 1$ in (3.20): when $F_h^{-1} < \omega_{max}/2$,

$$Ro^{-1} < -\tfrac{3}{2}\omega_{max} \quad \text{or} \quad Ro^{-1} > -\tfrac{1}{2}\omega_{max}, \tag{3.22}$$

and when $F_h^{-1} > \omega_{max}/2$,

$$-\tfrac{3}{2}\omega_{max} < Ro^{-1} < -\tfrac{1}{2}\omega_{max}. \tag{3.23}$$

Next, we consider the stability away from the elliptic stagnation points. The resonance condition is

$$\Omega_p^2 = (2\Omega_p + Ro^{-1})(\omega_z + Ro^{-1})\cos^2\theta + F_h^{-2}\sin^2\theta. \tag{3.24}$$

It is not elucidating to consider a solution to the above equation since Ω_p and ω_z depend on R differently. However, the case $\theta = 0°$, for which stratification effects vanish, turns out to be useful in interpreting the results in § 5. In this case, we have

$$\left(1 + \frac{Ro^{-1}}{2\Omega_p}\right)\left(\frac{\omega_z}{2\Omega_p} + \frac{Ro^{-1}}{2\Omega_p}\right) = \frac{1}{4}. \tag{3.25}$$

By noting that the vorticity ω_z decays more rapidly with R than Ω_p, which implies $\omega_z/2\Omega_p \le 1$, a solution to (3.25) for R exists when

$$-\frac{\omega_{max}}{2} \lesssim Ro^{-1} \lesssim 0. \tag{3.26}$$

Combined with (3.23), the instability condition for $F_h^{-1} > \omega_{max}/2$ becomes

$$-\tfrac{3}{2}\omega_{max} < Ro^{-1} \lesssim 0. \tag{3.27}$$

The dependence of the growth rate (3.21) on the parameters is not simple. We write $\sigma = C_E\varepsilon_e$, where C_E depends on Ro^{-1}, F_h^{-1} and ω_{max}. For the non-stratified case $F_h^{-1} = 0$, C_E decreases with Ro^{-1} when $Ro^{-1} > 0$; C_E increases with $|Ro^{-1}|$ when $-\omega_{max}/2 < Ro^{-1} < 0$.

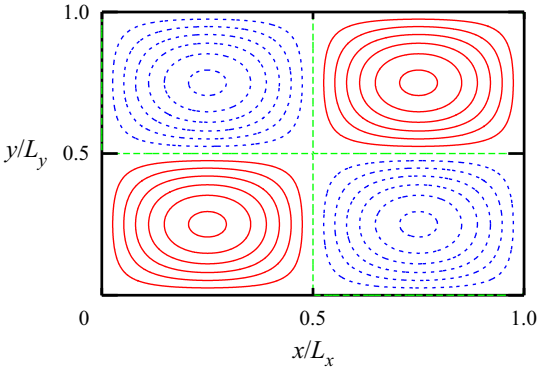

Figure 3. Streamlines of 2-D Taylor–Green vortices. $\varepsilon_e/\omega_{max} = 0.2$. The solid (red) and dashed (blue) lines correspond to positive and negative values of the stream function, respectively. The contour levels are $\Psi/\Psi_{max} = \pm 0.16, 0.32, \ldots, 0.96$.

4. Numerical procedure

4.1. *Base flow*

We choose the 2-D Taylor–Green vortices (figure 3) as a base flow as was done by Suzuki *et al.* (2018) and Hattori *et al.* (2021). The 2-D Taylor–Green vortices are an array of vortices doubly periodic in horizontal directions. The vorticity is

$$\omega(x, y) = \omega_{max} \sin \frac{2\pi x}{A} \sin 2\pi A y, \tag{4.1}$$

where A^2 is the ratio of the spatial period $L_x = A$ in x and $L_y = 1/A$ in y. Each vortex is contained in a rectangular cell where the vertices are hyperbolic points. The sign of vorticity in a cell is opposite to that in the neighbouring cells forming a staggered lattice of vortices. The vorticity is parallel to the vertical direction. The base flow is steady in the absence of viscous diffusion since the stream function

$$\Psi(x, y) = \frac{\omega_{max}}{(2\pi)^2 (A^2 + A^{-2})} \sin \frac{2\pi x}{A} \sin 2\pi A y, \tag{4.2}$$

satisfies (2.5) with (4.1).

Scaling and the base-flow parameter have been chosen as in our previous work (Suzuki *et al.* 2018; Hattori *et al.* 2021) for comparison purposes. Namely, the characteristic length has been set to the geometric mean of the rectangular cell $L_0 = (L_x L_y)^{1/2}/2 = 1$, while the characteristic velocity has been chosen as

$$U_0 = \frac{\omega_{max} L_0}{2\pi} = 1. \tag{4.3}$$

Two cases are considered: (i) $A = 1$, which implies $L_x = L_y$ and $\varepsilon_e/\omega_{max} = 0$, and (ii) $A = (7/3)^{1/4}$, which implies $L_x/L_y = \sqrt{7/3}$ and $\varepsilon_e/\omega_{max} = 0.2$. Other choices of scaling are possible; for example, the Rossby number and the Froude number are divided by 2π if we choose ω_{max}, as the time scale as was done by Sipp *et al.* (1999).

4.2. *Local stability analysis*

The numerical method for local stability analysis is essentially the same as that of Suzuki *et al.* (2018) except that the Coriolis force is taken into account in the present work.

Equations (2.15)–(2.18) were integrated in time by the fourth-order Runge–Kutta method. We consider periodic orbits of fluid particles throughout this paper. We also assume that the wavevector $\boldsymbol{k}$ is time-periodic which is a necessary condition for exponential instability on the periodic orbits. It is known that $\boldsymbol{k}$ is time-periodic if it is perpendicular to the streamline initially:

$$\boldsymbol{k}(0) \cdot \boldsymbol{u}_b(\boldsymbol{X}(0)) = 0. \tag{4.4}$$

Then the time evolution of amplitude is described by a Floquet matrix $\boldsymbol{F}$ since the matrices which appear in (2.17) is also time-periodic:

$$\{\boldsymbol{a}, r\}(t+T) = \boldsymbol{F}(T)\{\boldsymbol{a}, r\}(t), \tag{4.5}$$

where T is the period of $\boldsymbol{k}$ which coincides with that of the particle motion $\boldsymbol{X}$. Our task is to calculate the eigenvalues $\{\mu_i\}$ of $\boldsymbol{F}(T)$ which determines the growth rate as

$$\sigma_i = \frac{\log|\mu_i|}{T}. \tag{4.6}$$

Given the strength of rotation and stratification by the Rossby number Ro and the Froude number F_h, the initial conditions should be specified to have particular solutions. Among the initial conditions, one parameter, which is denoted by β in the following sections, is required for $\boldsymbol{X}(0)$ to identify a streamline in a 2-D flow. We set

$$\boldsymbol{X}(0) = \left(\frac{L_x}{4}(1-\beta), \frac{L_y}{4}, 0\right)^{\mathrm{T}}, \quad 0 \le \beta < 1. \tag{4.7}$$

The elliptic stagnation point corresponds to $\beta = 0$, while $\beta = 1$ corresponds to the cell boundaries.

Another parameter is required for $\boldsymbol{k}(0)$ to specify the direction of the wavevector which satisfies (4.4); we take the angle between $\boldsymbol{e}_z$ and $\boldsymbol{k}(0)$, which is denoted by θ_0. It should be pointed out that the magnitude of $\boldsymbol{k}(0)$ is arbitrary since the right-hand side of (2.17) depends only on the direction of $\boldsymbol{k}$ and is independent of the magnitude after taking the short-wave limit. For the amplitudes $\boldsymbol{a}(0)$ and $r(0)$, three independent initial conditions satisfying the incompressibility condition $\boldsymbol{a}(0) \cdot \boldsymbol{k}(0) = 0$ are considered; the results do not depend on the choice of the initial conditions since the space spanned by the three initial conditions is common. As a result, we obtain the largest growth rate σ as a function of β, θ_0, Ro and F_h: $\sigma = \sigma(\beta, \theta_0, Ro, F_h)$.

4.3. *Modal stability analysis*

In the modal stability analysis, (2.9)–(2.11) were solved numerically by the Fourier spectral method (Peyret 2010) assuming periodic boundary conditions in all three directions, as was done by Hattori *et al.* (2021). The time marching was performed by the fourth-order Runge–Kutta method.

Since the base flow is 2-D, the time evolution of disturbances is separable in the vertical direction. Thus, we set

$$\boldsymbol{u}' = \mathrm{e}^{\mathrm{i}k_z z} \sum_{k_x=-K_x}^{K_x} \sum_{k_y=-K_y}^{K_y} \tilde{\boldsymbol{u}}_{k_x,k_y} \exp(\mathrm{i}[k_x(x/L_x) + k_y(y/L_y)]) \tag{4.8}$$

with similar expression for p' and ρ'. The number of the Fourier modes is 500×500, the same as in the study by Hattori *et al.* (2021).

The growth rate and frequency were obtained by the method of Krylov subspace (Edwards *et al.* 1994; Julien, Ortiz & Chomaz 2004; Donnadieu *et al.* 2009; Hattori *et al.* 2021). Starting from randomized initial conditions, (2.9)–(2.11) were integrated for a certain long time. Intermediate states $\{(\boldsymbol{u}'(T_0), \rho'(T_0)), (\boldsymbol{u}'(T_0 + \Delta T), \rho'(T_0 + \Delta T)), \ldots, (\boldsymbol{u}'(T_0 + (N_K - 1)\Delta T), \rho'(T_0 + (N_K - 1)\Delta T))\}$ were used as generators of the Krylov subspace. Then the eigenvalues and the eigenmodes were obtained in the N_K-dimensional Krylov subspace.

In this method, the error of an eigenvalue λ of a linear operator $\boldsymbol{L}$ can be evaluated by

$$\epsilon = \frac{\|\boldsymbol{L}\boldsymbol{v} - \lambda \boldsymbol{v}\|}{\|\boldsymbol{v}\|}, \tag{4.9}$$

where $\boldsymbol{v}$ is the corresponding approximate eigenvector. The error ϵ depends on the initial time of the data T_0, the interval between the data ΔT and the dimension of the Krylov subspace N_K. To obtain eigenvalues accurately, several Krylov subspaces were generated from different sets of parameters and the eigenvalue with the smallest error for each eigenmode was chosen. The actual values of the parameters were chosen after trial and error. The number of data N_K was fixed to 10, the start time of the data was $T_0 = 195$ or 245 and the interval between the data ΔT was fixed to 5. Typically, the error of the eigenvalue is $\epsilon = O(10^{-10})$ for the largest eigenvalue for a fixed wavenumber k_z, while it increases for subdominant eigenmodes. In the following, we discarded the eigenmodes with $\epsilon \geq 10^{-3}$.

4.4. *Realizability as a mode*

As we see in § 5, the instabilities found by local stability analysis are not always found in modal stability analysis at finite Reynolds numbers since high-wavenumber modes are damped by viscous damping. In this case, the corresponding region of the instability in the (β, θ_0) plane is often thin so that it is difficult to construct an unstable mode. It is worth noting that Bayly (1988) derived a condition for construction of an unstable eigenmode from local solutions of the form (2.12)–(2.14); the spatial width of the mode is approximately $[-\sigma''(\beta)/2C(\beta)]^{-1/4}$, where $C(\beta)$ is an integral along a streamline and $C(\beta) > 0$ is the condition since $\sigma''(\beta)$ is normally negative. When $|\sigma''(\beta)|$ is small, the unstable region in the local stability analysis is wide and the corresponding mode has a large spatial width; in other words, the radial wavenumber of the mode is small. Therefore, the eigenmode corresponding to a wider unstable region in the (β, θ_0) plane is less affected by viscous damping. Moreover, if the unstable region is wide in the θ_0 direction, an eigenmode constructed by superposition of the local solutions can avoid viscous damping at lower Reynolds numbers.

With the above in mind, we intuitively introduce the following quantity:

$$\mathcal{R} = \int_S \sigma \sin\theta_0 \, \mathrm{d}\beta \, \mathrm{d}\theta_0, \tag{4.10}$$

where S is the region of an instability on the (β, θ_0) plane, to quantify *realizability* as a mode of each instability; eigenmodes corresponding to an unstable region may not be found at finite Reynolds numbers and finite wavenumbers if $\mathcal{R}$ is small. It should be noted that existence of a mode depends on the Reynolds number; the critical Reynolds number at which a particular mode appears would increase as $\mathcal{R}$ decreases. In the above definition of realizability $\mathcal{R}$, the factor $\sin\theta_0$ is required to account for the solid angle since θ_0 is the polar angle of a wavevector from the vertical axis in three dimensions. It should be pointed

out that this is a crude approximation; for example, it would be better to replace θ_0 by the average of θ. However, it is sufficient to interpret the results of modal stability analysis since only the order of magnitude of $\mathcal{R}$ matters.

5. Results

In this section, we show the results of local and modal stability analysis of the 2-D Taylor–Green vortices.

5.1. *Results of local stability analysis*

First, we show how each instability appears in local stability analysis by observing the growth rate $\sigma(\beta, \theta_0, Ro, F_h)$ as a function of β and θ_0 for given values of Ro and F_h. We choose the values of Ro and F_h to cover nearly all conditions for the instabilities in table 1: $F_h^{-1} = 0(< \omega_{max}/2)$ and $5(> \omega_{max}/2)$, and $|Ro^{-1}| = 0, 2(< \varepsilon_h, \omega_{max}/2)$ and $|Ro^{-1}| = 4(> \varepsilon_h, \omega_{max}/2)$ (also see table 2).

Figure 4 shows $\sigma(\beta, \theta_0, Ro, F_h)$ for the non-stratified case $F_h^{-1} = 0$, comparing among the Rossby numbers $Ro^{-1} = 0, \pm 2$ and ± 4. Four types of instability are observed: pure hyperbolic instability, centrifugal instability, rotational-hyperbolic instability and elliptic instability. The pure hyperbolic instability appears for $Ro^{-1} = \pm 2$ near $\beta = 1$ (figure 4*c*,*d*,*g*,*h*). The growth rate is the largest at $\theta_0 = 0^\circ$, while the unstable region extends to large θ_0. It does not appear for $Ro^{-1} = 0$ since the stretching near a hyperbolic stagnation point is cancelled by the compression near the next hyperbolic stagnation point, as explained by Suzuki *et al.* (2018). The centrifugal instability appears for $Ro^{-1} = -4$ as a band $0.6 \lesssim \beta \lesssim 0.8$ (figure 4*a*,*b*). The growth rate is the largest at $\theta_0 = 0^\circ$, while the unstable region extends to large θ_0 as in the case of the pure hyperbolic instability. The rotational-hyperbolic instability is observed for $Ro^{-1} = 4$ (figure 4*i*,*j*). The unstable region emanates from $(\beta, \theta_0) = (1, 90^\circ)$, becomes thick at $\beta \approx 0.9$ and then shrinks as β decreases. The elliptic instability appears for $\varepsilon_e/\omega_{max} = 0.2$ (figure 4*b*,*d*,*f*,*h*,*j*). It forms a horizontal band emanating from $(\beta, \theta_0) \approx (0, 60^\circ)$ for $Ro^{-1} = 0$ (figure 4*f*). The band moves to larger θ_0 for $Ro^{-1} > 0$ (figure 4*h*,*j*), while it becomes wide for $Ro^{-1} = -2$ (figure 4*d*). The unstable region survives with reduced growth rate near $(\beta, \theta_0) = (0, 0)$ for $Ro^{-1} = -4$ (figure 4*b*), although the elliptic instability does not occur according to table 1; the lower limit of Ro^{-1} for the elliptic instability is -4.3, as shown later in figure 6, which is larger in magnitude than the limit $-\omega_{max}/2 = -3.14$. The only remarkable difference between $\varepsilon_e/\omega_{max} = 0$ and 0.2 is that the elliptic instability appears for $\varepsilon_e/\omega_{max} = 0.2$. The characteristic features of each instability for $\varepsilon_e/\omega_{max} = 0.2$ are in good agreement with Sipp *et al.* (1999) for $\varepsilon_e/\omega_{max} = 0.3$ ($L_x/L_y = 2$). The rotational-hyperbolic instability was observed as many thin bands by Godeferd *et al.* (2001) for the Stuart vortices; in the present case, the number of bands is small owing to the difference in vorticity distribution.

Figure 5 shows the growth rate $\sigma(\beta, \theta_0, Ro, F_h)$ for a stratified case $F_h^{-1} = 5$. There are several differences from $F_h^{-1} = 0$. The strato-hyperbolic instability appears for $Ro^{-1} = 0, \pm 2$ (figure 5*c*–*h*). The elliptic instability is stabilized for $Ro^{-1} \geq 0$, while it survives for $Ro^{-1} = -2$ and -4, as predicted in § 3.5. It is pointed out that the unstable region of the elliptic instability for $Ro^{-1} = -4$ is larger than that of the non-stratified case (figure 4*b*). The rotational-hyperbolic instability is hardly visible as the growth rate decreases significantly. Most of the unstable regions are compressed to $\theta_0 = 0^\circ$ by stratification; at $\theta_0 = 0^\circ$, however, the effects of stratification vanish according to (2.29)

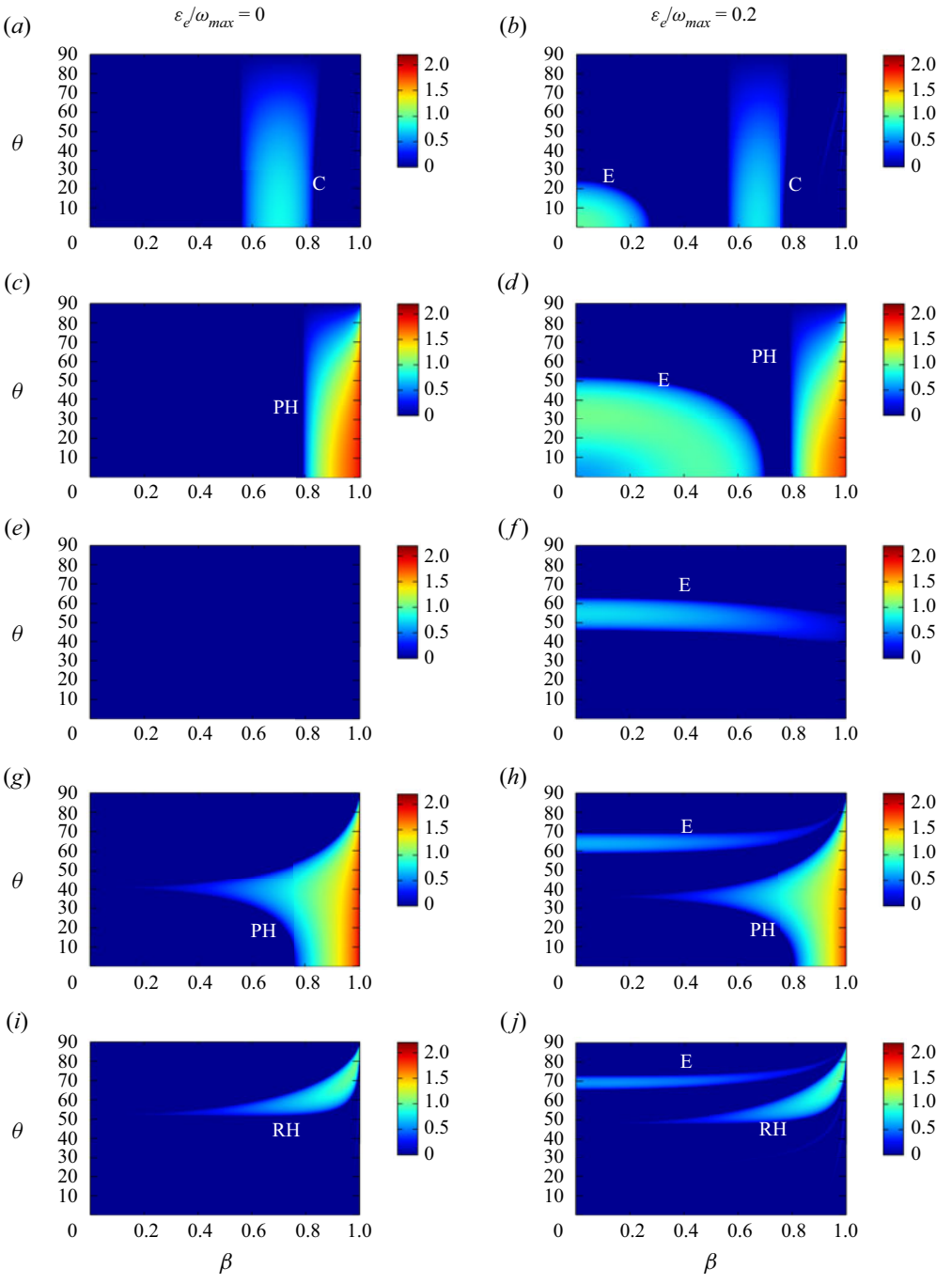

Figure 4. Growth rate $\sigma(\beta, \theta_0, Ro, F_h)$ as a function of β and θ_0 obtained by local stability analysis. $F_h^{-1} = 0$ and (*a*,*c*,*e*,*g*,*i*) $\varepsilon_e/\omega_{max} = 0$ and (*b*,*d*,*f*,*h*,*j*) 0.2. $Ro^{-1} =$ (*a*,*b*) −4, (*c*,*d*) −2, (*e*,*f*) 0, (*g*,*h*) 2, (*i*,*j*) 4.

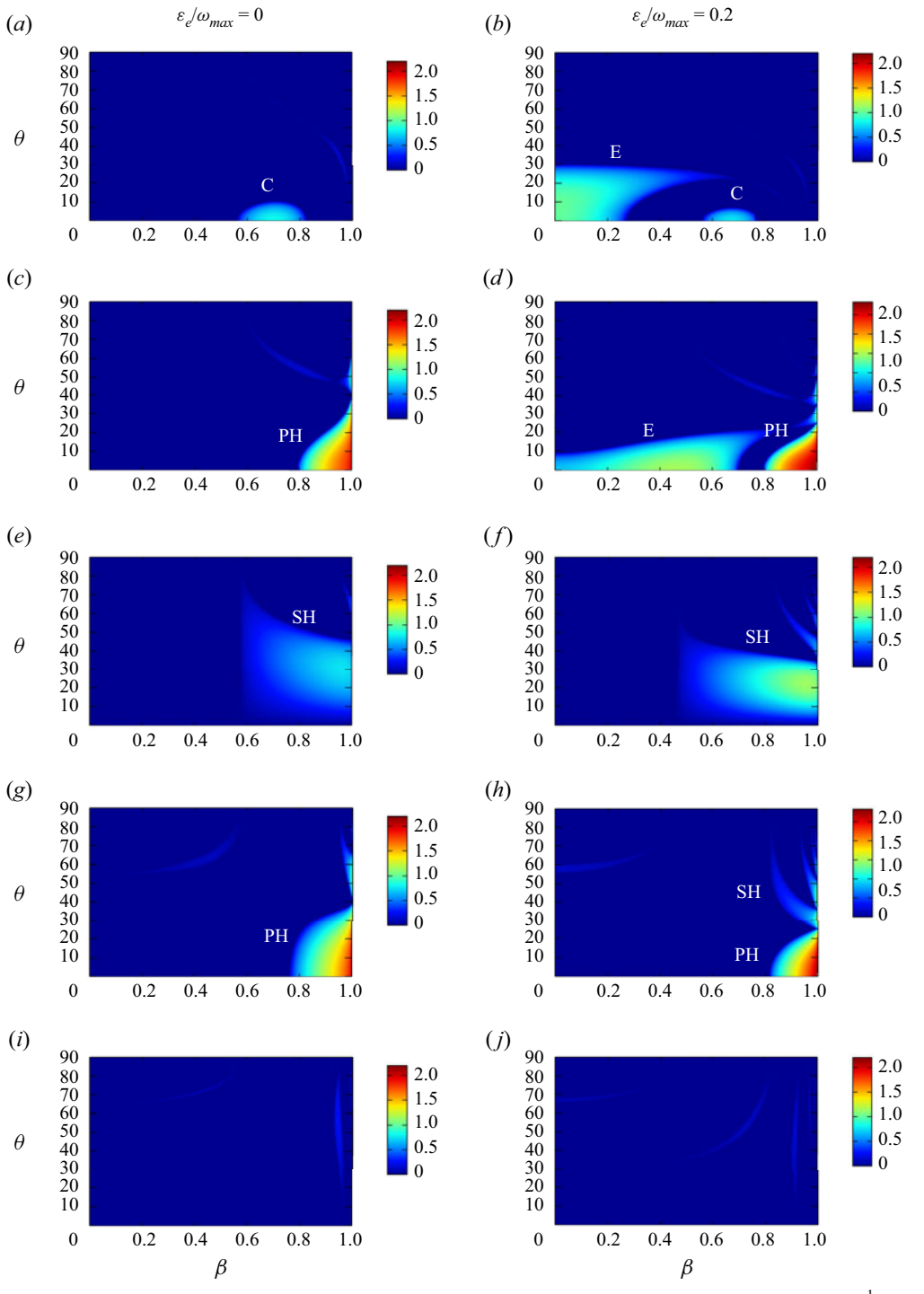

Figure 5. Growth rate $\sigma(\beta, \theta_0, Ro, F_h)$ as a function of β and θ_0 obtained by local stability analysis. $F_h^{-1} = 5$ and (*a*,*c*,*e*,*g*,*i*) $\varepsilon_e/\omega_{max} = 0$ and (*b*,*d*,*f*,*h*,*j*) 0.2. $Ro^{-1} =$ (*a*,*b*) −4, (*c*,*d*) −2, (*e*,*f*) 0, (*g*,*h*) 2, (*i*,*j*) 4.

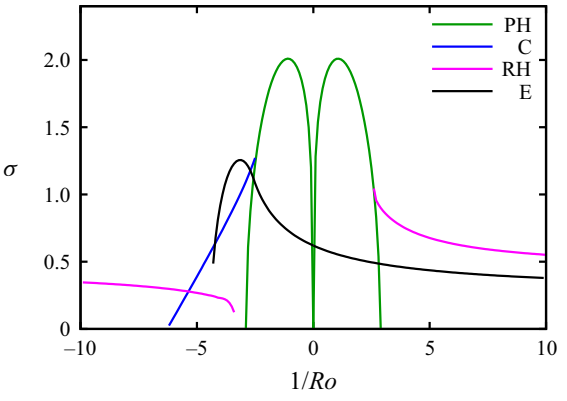

Figure 6. Growth rate $\sigma_{max}(Ro, F_h)$ as a function of Ro obtained by local stability analysis. $\varepsilon_e/\omega_{max} = 0.2$, $F_h^{-1} = 1$.

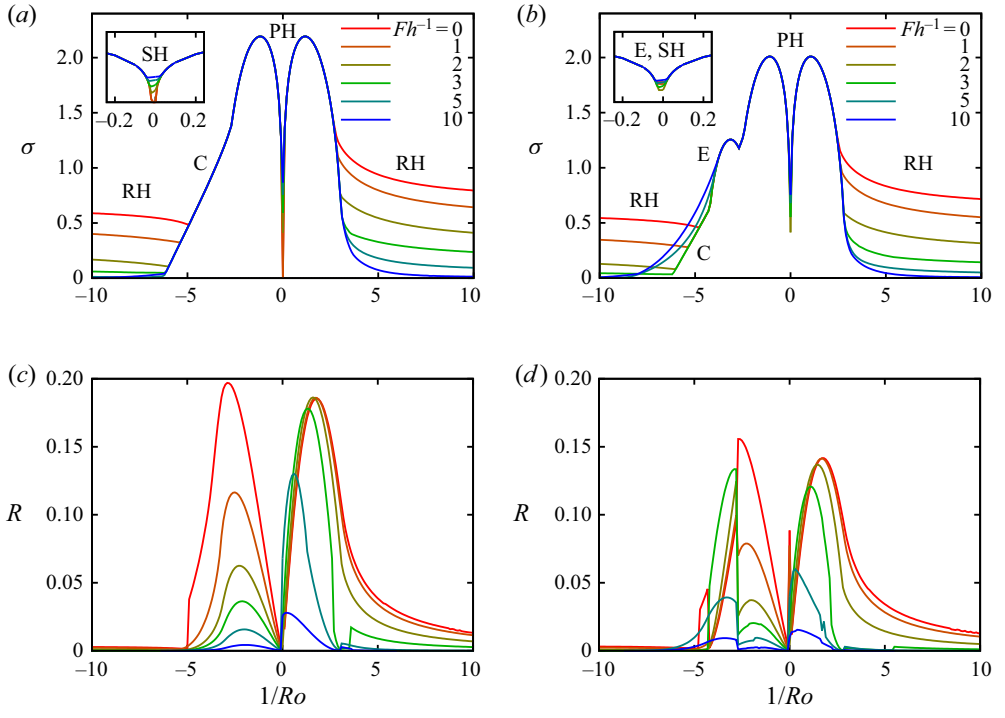

Figure 7. (*a*,*b*) Growth rate $\sigma_{max}(Ro, F_h)$ and (*c*,*d*) realizability as a function of Ro^{-1} obtained by local stability analysis. Also shown as insets in (*a*,*b*) are close-up views of the growth rate $\sigma_{max}(Ro, F_h)$ for weak rotation $-0.25 \leq Ro^{-1} \leq 0.25$. (*a*,*c*) $\varepsilon_e/\omega_{max} = 0$, (*b*,*d*) $\varepsilon_e/\omega_{max} = 0.2$.

and (2.30). As a result, the maximum growth rates of the pure hyperbolic instability and the centrifugal instability are the same as those for $F_h^{-1} = 0$.

To elucidate which instability is dominant and how it depends on stratification and rotation, we focus on the maximum growth rate for fixed magnitude of rotation and stratification in the rest of this subsection: $\sigma_{max}(Ro, F_h) = \max_{\beta,\theta_0} \sigma(\beta, \theta_0, Ro, F_h)$. Figure 6 shows $\sigma_{max}(Ro, F_h)$ as a function of Ro^{-1} for $(\varepsilon_e/\omega_{max}, F_h^{-1}) = (0.2, 1)$. In

this figure, maximum is taken for each instability. The four types of instability are observed as in figure 4. Important features of each instability are captured. For example, the pure hyperbolic instability appears for $|Ro^{-1}| \lesssim 2.9$. It is worth noting that the growth rate is nearly the same for cyclonic and anti-cyclonic rotation; this is because the pure hyperbolic instability occurs near the cell boundaries where vorticity is weak. The centrifugal instability appears for $-6.2 \lesssim Ro^{-1} \lesssim -2.7$ bifurcating from the pure hyperbolic instability; rigorously speaking, it is difficult to distinguish between the pure hyperbolic instability and the centrifugal instability for $-2.7 \lesssim Ro^{-1} < 0$. In figure 7, we show how the maximum growth rate $\sigma_{max}(Ro, F_h)$ depends not only on rotation but also on stratification; $\sigma_{max}(Ro, F_h)$ is plotted against Ro^{-1} for selected values of F_h^{-1}, while the close-up view of $\sigma_{max}(Ro, F_h)$ for weak rotation $|Ro^{-1}| \leq 0.25$ is shown in the insets. Also shown in this figure is the realizability $\mathcal{R}$ introduced by (4.10). Each curve for a fixed value of F_h^{-1} consists of different types of instability, as observed in figure 6. The dominant instability for $\varepsilon_e/\omega_{max} = 0$ changes as

$$Ro^{-1} \geq 0: \quad (\mathrm{SH} \rightarrow)\ \mathrm{PH} \rightarrow \mathrm{RH}, \tag{5.1}$$

$$Ro^{-1} \leq 0: \quad (\mathrm{SH} \rightarrow)\ \mathrm{PH} \rightarrow \mathrm{C} \rightarrow \mathrm{RH} \tag{5.2}$$

as $|Ro^{-1}|$ increases, and for $\varepsilon_e/\omega_{max} = 0.2$ as

$$Ro^{-1} \geq 0: \quad (\mathrm{E/SH} \rightarrow)\ \mathrm{PH} \rightarrow \mathrm{RH}, \tag{5.3}$$

$$Ro^{-1} \leq 0: \quad (\mathrm{E/SH} \rightarrow)\ \mathrm{PH} \rightarrow \mathrm{E}\ (\rightarrow \mathrm{C}) \rightarrow \mathrm{RH}, \tag{5.4}$$

where occurrence of the parenthesized instabilities depends on the magnitude of stratification. We see that the pure hyperbolic instability and the centrifugal instability are unaffected by stratification in figure 7 since the maximum occurs at $\theta_0 = 0^\circ$. This does not imply that the actual unstable modes are also independent of stratification since stratification affects mode structures; in fact, realizability $\mathcal{R}$ decreases as F_h^{-1} increases (figure 7*c*,*d*), which is more prominent for the anti-cyclonic case ($Ro^{-1} < 0$) than for the cyclonic case ($Ro^{-1} > 0$). However, the rotational-hyperbolic instability and the elliptic instability are strongly affected by stratification. The rotational-hyperbolic instability appears for $Ro^{-1} \gtrsim 3$ bifurcating from the pure hyperbolic instability, while it also appears for $Ro^{-1} \lesssim -4$. The growth rate and the realizability decrease as stratification becomes strong; $\mathcal{R}$ almost vanishes for $Ro^{-1} < 0$, suggesting that it is difficult to observe the corresponding unstable modes at finite Reynold numbers. The growth rate of the elliptic instability, which appears only for $\varepsilon_e/\omega_{max} = 0.2$, becomes maximum at $Ro^{-1} \approx -3.1$. The unstable range is different for $F_h^{-1} \leq 3$ and $F_h^{-1} \geq 5$, as predicted in § 3.5. The growth rate decreases with F_h^{-1} for $Ro^{-1} > 0$ and increases with F_h^{-1} for $Ro^{-1} \lesssim -4$, whereas the maximum growth rate at $Ro^{-1} \approx -3.1$ does not depend on stratification. The strato-hyperbolic instability appears for $F_h^{-1} \gtrsim 2$; it merges with the pure hyperbolic instability at $Ro^{-1} \approx 0.03$. The growth rate decreases with rotation for $Ro^{-1} < 0$.

It is of interest to evaluate the coefficients of the growth rate in table 1. Figure 8 shows the coefficient as a function of Ro^{-1} for each instability. Since the coefficients C_{PH} and C_C are independent of stratification, they are compared between $\varepsilon_e/\omega_{max} = 0$ and 0.2 (figure 8*a*,*b*). We observe that the difference between the cases $\varepsilon_e/\omega_{max} = 0$ and 0.2 are small; it is also the case for the the strato-hyperbolic instability and the rotational-hyperbolic instability, while the coefficient of the elliptic instability vanishes for $\varepsilon_e/\omega_{max} = 0$. Thus, the coefficients of the strato-hyperbolic instability, the

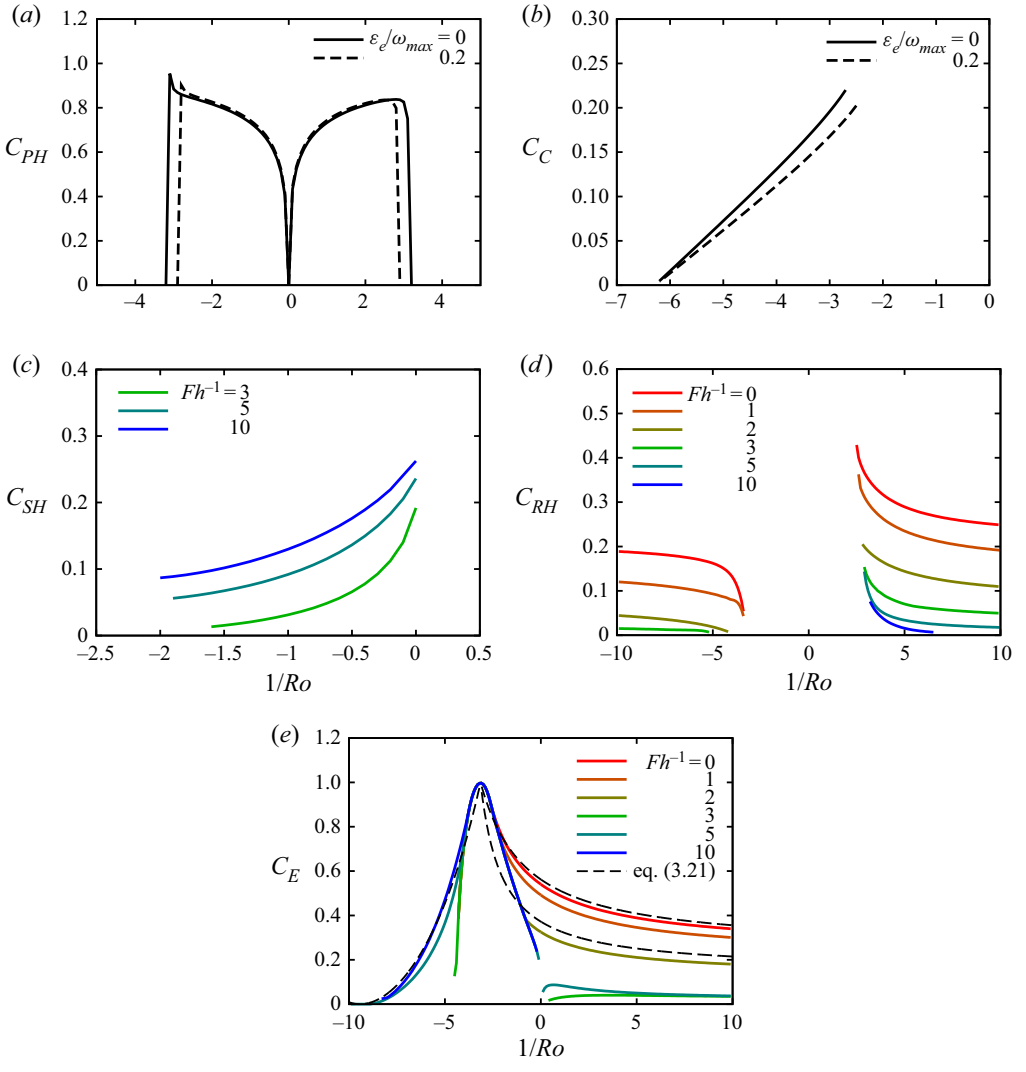

Figure 8. Coefficients which appear in table 1 as a function of Ro^{-1} obtained by local stability analysis. Panels (*a*,*b*) shows C_{PH} and C_C, respectively, for $\varepsilon_e/\omega_{max} = 0$ and 0.2. Panels (*c*–*e*) shows C_{SH}, C_{RH} and C_E for $F_h^{-1} = 0$, 1, 2, 3, 5 and 10, while $\varepsilon_e/\omega_{max}$ is fixed to 0.2. The dashed lines in (*e*) show the analytical values (3.21) for $F_h^{-1} = 0$, 2 and 10.

rotational-hyperbolic instability and the elliptic instability are shown for the same values of F_h^{-1} as in figure 7 with $\varepsilon_e/\omega_{max} = 0.2$ (figure 8*c*,*d*,*e*). The magnitude of the coefficients is $O(1)$ for all instabilities, while it is small for the centrifugal instability and the strato-hyperbolic instability.

Figure 8 reveals some features of subdominant modes which are not shown in figure 7. The coefficient of the strato-hyperbolic instability C_{SH} vanishes for $F_h^{-1} \leq 2$; it increases with F_h^{-1}. The coefficient of the elliptic instability is maximum $C_E = 1.0$ at $Ro^{-1} = -3.1$; it is independent of stratification for $-3.7 \lesssim Ro^{-1} \lesssim -2.7$, where the maximum growth rate occurs at $\theta_0 = 0$. Also shown in figure 8(*e*) by the dashed lines is the analytical growth

rate (3.21) for $F_h^{-1} = 0$, 2 and 10. It is in good agreement with the numerical results except for intervals near $Ro^{-1} = -3.1$ where $\theta_0 = 0$.

Figure 8 also helps us deduce how the coefficients depend on the Rossby number. The coefficients C_{PH} and C_{RH} do not depend on Ro^{-1} significantly except for $Ro^{-1} \approx 0$ for C_{PH}, and for $Ro^{-1} \approx 3$ and -4 for C_{RH}. The coefficient of the centrifugal instability decreases with $|Ro^{-1}|$ as the unstable region moves to small β; this is understood by the expression of the growth rate (3.13) since the difference between $2\Omega_p$ and ω_z decreases as β decreases. Figure 8(*b*) suggests that the relation between C_C and Ro^{-1} can be approximated as

$$C_C \propto 1 - \frac{|Ro^{-1}|}{\omega_{max}}, \tag{5.5}$$

which can be applicable when vorticity is non-negative and decreases monotonically with β. However, it is not easy to find an explicit relation analytically since it depends on the velocity distribution of the vortex in a nonlinear way.

The numerical results obtained by local stability analysis in this subsection are in good agreement with predictions in § 3. Occurrence of each instability, its growth rate and their dependence on rotation and stratification have been elucidated in detail. However, these results should be checked by modal stability analysis, as is done in the next subsection.

5.2. *Results of modal stability analysis*

In this subsection, we show the results of modal stability analysis of the 2-D Taylor–Green vortices. Two remarks are made before presenting the results. One is about symmetry of the modes. The 2-D Taylor–Green vortices possess several symmetries in the absence of rotation (Sipp *et al.* 1999; Suzuki *et al.* 2018; Hattori *et al.* 2021). However, rotation breaks mirror symmetry with respect to $x = mL_x/2$ and $y = nL_y/2$, where m and n are integers. The symmetries that survive under rotation are translations $(x, y; \omega_z) \to (x + n(L_x/2), y \pm n(L_y/2); \omega_z)$ and a π rotation $(x, y; \omega_z) \to (-x, -y; \omega_z)$. Thanks to the latter symmetry, the unstable modes can be classified into symmetric and anti-symmetric modes: the mode is symmetric when it satisfies

$$u'(-x, -y, z) = -u'(x, y, z), \quad v'(-x, -y, z) = -v'(x, y, z), \tag{5.6a,b}$$

$$w'(-x, -y, z) = w'(x, y, z), \quad \rho'(-x, -y, z) = \rho'(x, y, z), \tag{5.7a,b}$$

while it is anti-symmetric when it satisfies

$$u'(-x, -y, z) = u'(x, y, z), \quad v'(-x, -y, z) = v'(x, y, z), \tag{5.8a,b}$$

$$w'(-x, -y, z) = -w'(x, y, z), \quad \rho'(-x, -y, z) = -\rho'(x, y, z). \tag{5.9a,b}$$

One of the above sets of conditions was imposed to obtain the modes of each symmetry separately. The other remark is that we cannot distinguish between the cyclonic ($Ro > 0$) and the anti-cyclonic ($Ro < 0$) modes rigorously; since the 2-D Taylor–Green vortices consist of vortices with positive vorticity and those with negative vorticity located in a staggered arrangement, the unstable modes have non-vanishing amplitudes both in the cyclonic vortices and in the anti-cyclonic vortices in general. This is indeed the case for weak rotation; as wee see below, however, the modes are nearly cyclonic or anti-cyclonic when rotation is strong. To see whether the mode is cyclonic, anti-cyclonic or in-between,

we define the enstrophy ratio by

$$\phi = \frac{\Phi_1}{\Phi_1 + \Phi_2}, \quad \Phi_i = \int_{D_i} |\boldsymbol{\omega}'|^2 \, \mathrm{d}x \, \mathrm{d}y \, \mathrm{d}z, \tag{5.10a,b}$$

where D_1 and D_2 are the domains occupied by anti-clockwise and clockwise vortices, respectively,

$$D_i = \left\{ (x, y, z) \mid \frac{\mathrm{i} - 1}{2} \leq \frac{x}{L_x} \leq \frac{\mathrm{i}}{2}, \ 0 \leq \frac{y}{L_y} \leq \frac{1}{2}, \ 0 \leq \frac{z}{L_z} \leq 1 \right\}. \tag{5.11}$$

The mode is nearly cyclonic when ϕ is close to 1, while it is anti-cyclonic when ϕ is close to 0, because the sense of rotation of the system is set anti-clockwise in the following analysis.

In the modal stability analysis, the growth rate is a multi-valued function of the vertical wavenumber k_z, the Rossby number Ro and the Froude number F_h: $\sigma = \sigma(k_z, Ro, F_h)$. Based on the local stability results, the strength of rotation is chosen from $|Ro^{-1}| = 0, 1, \ldots, 4$, while one case of vanishing or weak stratification $F_h^{-1} < \omega_{max}/2$ and another case of strong stratification $F_h^{-1} > \omega_{max}/2$ are chosen: $F_h^{-1} = 0$ and 5 for $\varepsilon_e/\omega_{max} = 0$, and $F_h^{-1} = 1$ and 5 for $\varepsilon_e/\omega_{max} = 0.2$. A few other cases were also considered, but the above sets of parameter values proved sufficient to elucidate the effects of rotation and stratification. The Reynolds number is fixed to $Re = 10^5$. In the following, all modes where structures are shown are non-oscillatory (i.e. the complex parts of the eigenvalues are zero), while there also exist oscillatory modes, which are sub-dominant.

5.2.1. $\varepsilon_e/\omega_{max} = 0$

First, we show the results for $\varepsilon_e/\omega_{max} = 0$ to show how each instability appears in modal stability analysis; the difference due to the symmetry of the modes is also checked. Figure 9 shows the growth rate plotted against the vertical wavenumber k_z in the absence of stratification ($F_h^{-1} = 0$). The results are shown for three values of the Rossby number: $|Ro^{-1}| = 0$, 2 and 4; for each value of $|Ro^{-1}|$, symmetric and anti-symmetric modes are shown separately. The line colours show the enstrophy ratio ϕ: cyclonic modes ($\phi = 1$) and anti-cyclonic modes ($\phi = 0$) are shown by red and blue lines, respectively. For $Ro^{-1} = 0$, one symmetric mode of the pure hyperbolic instability and one anti-symmetric mode of mixed hyperbolic instability (Hattori *et al.* 2021) are observed (figure 9*a*,*b*). Since the mirror symmetry with respect to $x = mL_x/2$ and $y = nL_y/2$ is preserved in the absence of rotation, the enstrophy ratio is $\phi = 0.5$ for these modes. For $|Ro^{-1}| = 2$, all modes are due to the pure hyperbolic instability; examples of mode structures are shown in figure 10. The maximum growth rate is $\sigma = 1.66$, which is larger than $\sigma = 0.449$ for $Ro^{-1} = 0$. Weak rotation breaks the balance between stretching and compression at the hyperbolic stagnation points so that many pure-hyperbolic-instability modes appear for $Ro^{-1} \neq 0$. There are a few differences between the symmetric and anti-symmetric modes. First, the growth rates of the anti-symmetric modes are larger than those of the symmetric modes. This is due to the symmetry conditions, which make the symmetric modes vanish at the hyperbolic stagnation points; correspondingly, the amplitude of the disturbances is small near the cell boundaries; in fact, the enstrophy ratio of symmetric modes is close to 0 or 1, while it takes intermediate values for the anti-symmetric modes. This reduces the growth rates of the symmetric modes (figure 9*c*) in comparison to the anti-symmetric modes (figure 9*d*) because the pure hyperbolic instability is due to stretching near the

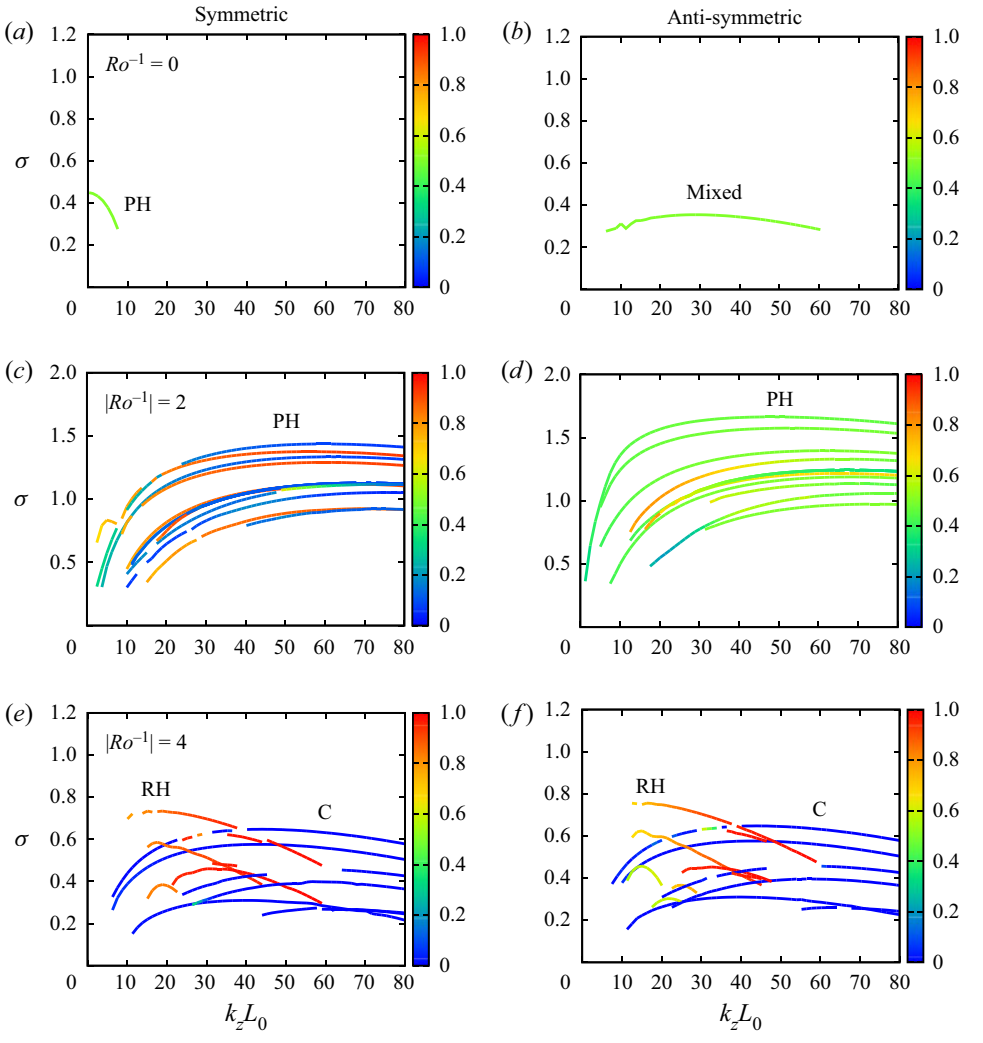

Figure 9. Growth rate $\sigma(k_z, Ro, F_h)$; $\varepsilon_e/\omega_{max} = 0$, $F_h^{-1} = 0$; $|Ro^{-1}| = (a,b)$ 0, (c,d) 2, (e,f) 4. (a,c,e) Symmetric modes, (b,d,f) anti-symmetric modes. The colour shows the enstrophy ratio ϕ.

hyperbolic points. The local stability results showed that the growth rate of the pure hyperbolic instability does not depend on the sense of rotation; this explains the presence of anti-symmetric modes which span both cyclonic and anti-cyclonic vortices with ϕ close to 0.5 (figure 10*b*).

The growth rates for stronger rotation $|Ro^{-1}| = 4$ (figure 9*e*,*f*) are smaller than those for $|Ro^{-1}| = 2$; the maximum is $\sigma = 0.756$, which is 45 % of that for $|Ro^{-1}| = 1$. In contrast to weaker rotation case $|Ro^{-1}| = 2$, there is little difference between the symmetric and anti-symmetric modes. This is because the amplitude of the modes is small near the cell boundaries so that they are unaffected by the symmetry conditions. The modes are nearly cyclonic (red, $\phi \approx 1$) or anti-cyclonic (blue, $\phi \approx 0$). The pure hyperbolic instability is absent. The cyclonic modes are due to the rotational-hyperbolic instability (figure 11*a*), while the anti-cyclonic modes are due to the centrifugal instability (figure 11*b*). The maximum growth rate of the rotational-hyperbolic instability occurs at $k_z L_0 = 16.3$, while that of the centrifugal instability occurs at $k_z L_0 = 44.0$. This difference can be explained

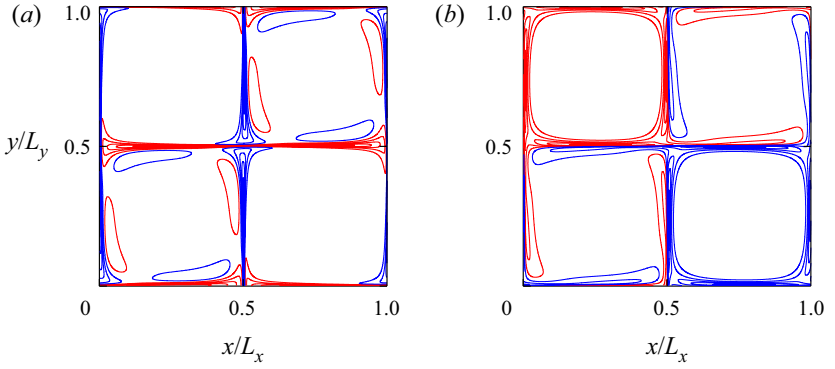

Figure 10. Mode structures shown by contours of ω_z' on the xy plane; $\varepsilon_e/\omega_{max} = 0, F_h^{-1} = 0$ and $|Ro^{-1}| = 1$. (*a*) Symmetric pure-hyperbolic-instability mode with $k_zL_0 = 62.8$, $\sigma = 1.40$ and $\phi = 0.925$, (*b*) anti-symmetric pure-hyperbolic-instability mode with $k_zL_0 = 62.8$, $\sigma = 1.73$ and $\phi = 0.554$. The contours of ω_z' are drawn for $|\omega_z'|/|\omega_z'|_{max} = 0.1, 0.3, 0.5, 0.7$ and 0.9; the red and blue lines correspond to positive and negative values, respectively.

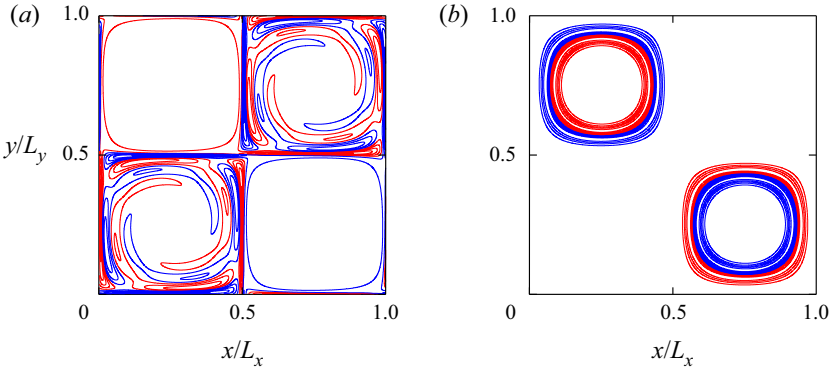

Figure 11. Mode structures shown by contours of ω_z' on the xy plane. 2-D Taylor–Green vortices with $\varepsilon_e/\omega_{max} = 0, F_h^{-1} = 0$ and $|Ro^{-1}| = 4$. (*a*) Anti-symmetric rotational-hyperbolic-instability mode with $k_zL_0 = 25.1$, $\sigma = 0.729$ and $\phi = 0.852$, (*b*) anti-symmetric centrifugal-instability mode with $k_zL_0 = 62.8$, $\sigma = 0.626$ and $\phi = 0$. The contours of ω_z' are drawn as in figure 10.

by the angle of the wavenumber vector at which the growth rate is maximum in the local stability analysis; θ_0 is close to 90° for the rotational-hyperbolic instability, while $\theta_0 = 0°$ for the centrifugal instability; if we assume that the magnitude k of the wavenumber vector is determined by the viscous diffusion and of the same order, then $k_z = k\cos\theta_0$ is larger for the centrifugal instability than for the rotational-hyperbolic instability. It is pointed out that there is no anti-cyclonic mode of the rotational-hyperbolic instability, for which the realizability $\mathcal{R}$ is small (figure 7*c*). Next, we show how stratification affects the stability properties. Figure 12 shows the growth rate plotted against the vertical wavenumber for the stratified case ($F_h^{-1} = 5$). For $Ro^{-1} = 0$ (figure 12*a*,*b*), several modes of the strato-hyperbolic instability and the mixed instability of the pure hyperbolic and strato-hyperbolic instabilities appear as both symmetric and anti-symmetric modes (Hattori *et al.* 2021).

For $|Ro^{-1}| = 2$ (figure 12*c*,*d*), all modes are due to the pure hyperbolic instability (figure 13). The growth rates of the anti-symmetric modes are slightly smaller than those

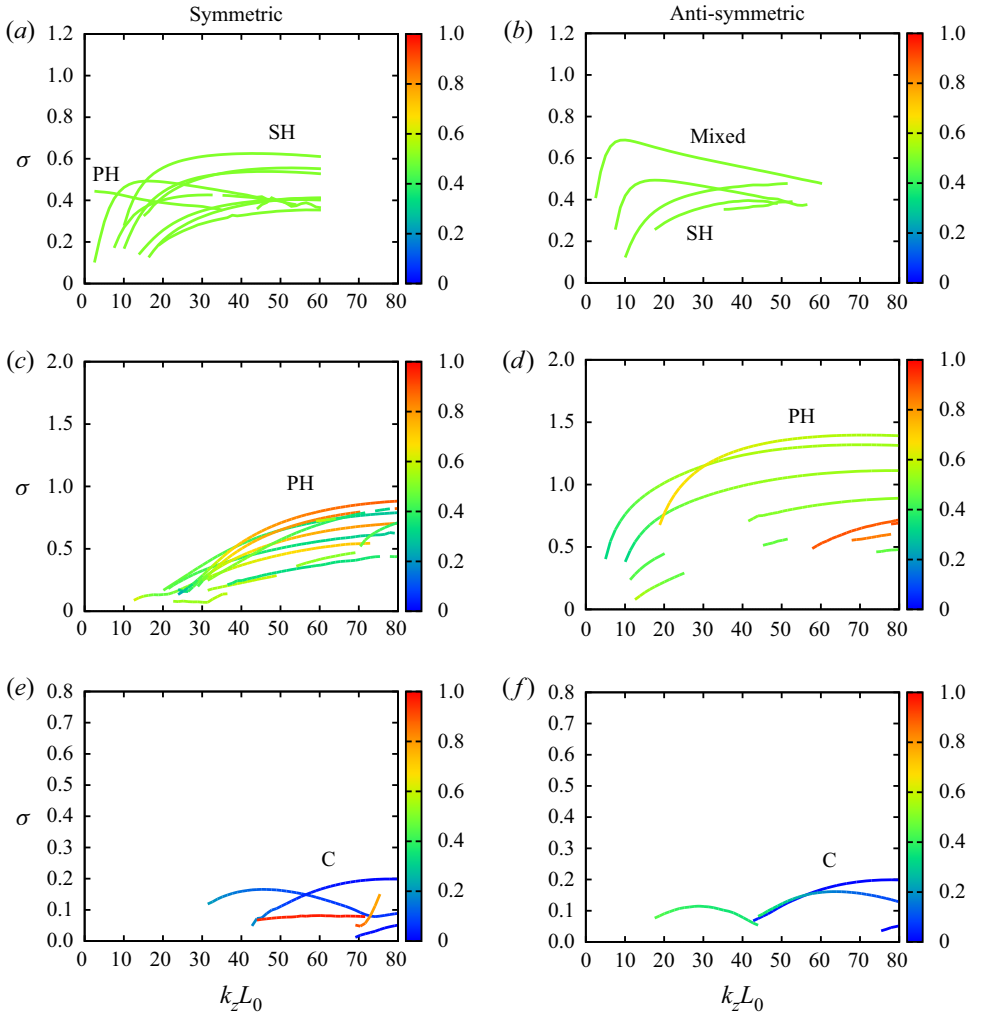

Figure 12. Growth rate $\sigma(k_z, Ro, F_h)$. Two-dimensional Taylor–Green vortices with $\varepsilon_e/\omega_{max} = 0$, $F_h^{-1} = 5$. $|Ro^{-1}| =$ (*a*,*b*) 0, (*c*,*d*) 2, (*e*,*f*) 4. (*a*,*c*,*e*) Symmetric modes, (*b*,*d*,*f*) anti-symmetric modes. The colour shows the enstrophy ratio ϕ.

for $F_h^{-1} = 0$, while the growth rates of the symmetric modes are further reduced. It is worth noting that the anti-cyclonic modes are nearly absent as the enstrophy ratio is larger than 0.5 for most of the branches; this is associated with the asymmetric reduction of realizability by stratification observed in figure 7(*c*,*d*). As shown in figure 13, stratification compresses the modes to flatten in the *xy* plane compared to the non-stratified case with the same wavenumber (figure 10) as observed in our previous work for the strato-hyperbolic instability (Hattori *et al.* 2021).

For $|Ro^{-1}| = 4$ (figure 12*e*,*f*), the growth rates are significantly reduced by stratification. There are no rotational-hyperbolic-instability modes; this is expected since the maximum growth rate as well as the realizability decrease with stratification according to the local stability analysis. The growth rate of the centrifugal instability is reduced in comparison to the non-stratified case, although the maximum growth rate obtained by

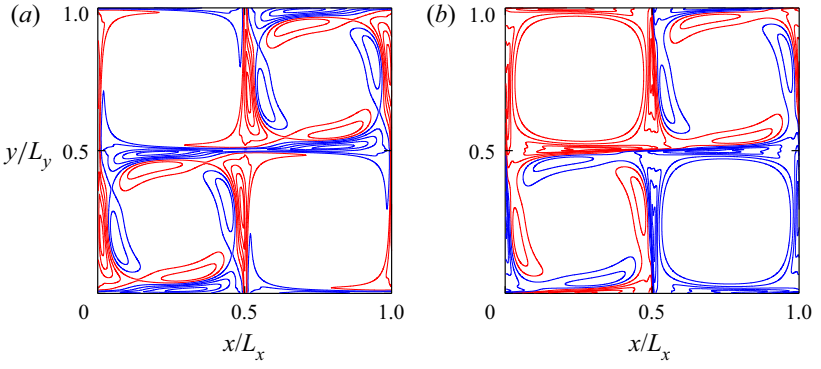

Figure 13. Mode structures shown by contours of ω_z' on the xy plane. Two-dimensional Taylor–Green vortices with $\varepsilon_e/\omega_{max} = 0$, $F_h^{-1} = 5$, $|Ro^{-1}| = 1$. (*a*) Symmetric pure-hyperbolic-instability mode with $k_zL_0 = 62.8$, $\sigma = 1.14$ and $\phi = 0.915$, (*b*) anti-symmetric pure-hyperbolic-instability-mode with $k_zL_0 = 62.8$, $\sigma = 1.44$ and $\phi = 0.722$. The contours of ω_z' are drawn as in figure 10.

local stability analysis does not depend on stratification. This point will be discussed later in § 5.3 (see also figure 18).

5.2.2. $\varepsilon_e/\omega_{max} = 0.2$

Next, we show the results for $\varepsilon_e/\omega_{max} = 0.2$ to see the effects of strain. We focus on the anti-symmetric modes below since the differences due to the symmetry are similar to the case of $\varepsilon_e/\omega_{max} = 0$.

Figure 14 shows the growth rate plotted against the vertical wavenumber k_z; the results for weak stratification ($F_h^{-1} = 1$) and strong stratification ($F_h^{-1} = 5$) are compared. For $Ro^{-1} = 0$, all modes are due to the elliptic instability for $F_h^{-1} = 1$ (figure 14*a*), while the elliptic instability is stabilized by stratification for $F_h^{-1} = 5$ (Suzuki *et al.* 2018) (figure 14*b*); the mixed-hyperbolic-instability modes and the strato-hyperbolic-instability modes are observed as in the case of $\varepsilon_e/\omega_{max} = 0$ and $F_h^{-1} = 5$.

For $|Ro^{-1}| = 2$ with $F_h^{-1} = 1$ (figure 14*c*), most of the modes are due to the pure hyperbolic instability (figure 15*a*), while some modes of the elliptic instability also exist (figure 15*b*). The magnitude of the growth rates is comparable to the case $\varepsilon_e/\omega_{max} = 0$ and $F_h^{-1} = 0$ (figure 9*a*,*b*). For $F_h^{-1} = 5$ (figure 14*d*), the pure-hyperbolic-instability modes also appear with reduced growth rates (figure 16*a*). The elliptic instability occurs for $|Ro^{-1}| = 2$ as anti-cyclonic modes (shown by blue lines in figure 14*d*).

For $|Ro^{-1}| = 4$ with $F_h^{-1} = 1$ (figure 14*e*), the rotational-hyperbolic instability appears at low wavenumbers $k_zL_0 \approx 30$ and the centrifugal instability appears for $k_zL_0 \gtrsim 20$ as in the case of $\varepsilon_e/\omega_{max} = 0$, $F_h^{-1} = 0$ and $|Ro^{-1}| = 4$, although the growth rates are smaller. An example of the rotational-hyperbolic-instability modes shown in figure 15(*c*) is similar to that for $\varepsilon_e/\omega_{max} = 0$ (figure 11*a*), while that of the centrifugal-instability modes shown in figure 15(*d*) is similar to that for $\varepsilon_e/\omega_{max} = 0$ (figure 11*b*) except for the aspect ratio in the xy plane. For $F_h^{-1} = 5$, however, most of the modes are due to the elliptic instability (figure 16*b*), while a few modes of the centrifugal instability are observed; no rotational-hyperbolic-instability mode is observed. These are in accordance with the local stability results.

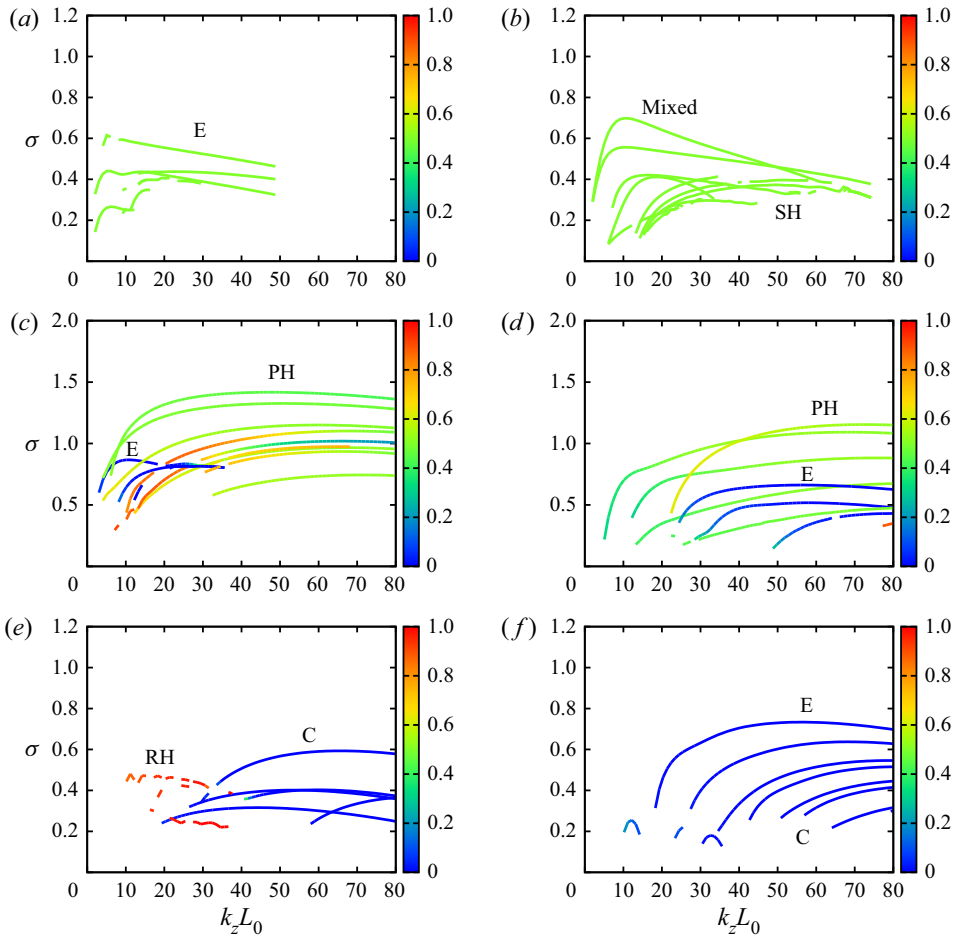

Figure 14. Growth rate $\sigma(k_z, Ro, F_h)$. Two-dimensional Taylor–Green vortices with $\varepsilon_e/\omega_{max} = 0.2$. $|Ro^{-1}| = (a,b)$ 0, (c,d) 2, (e,f) 4. (a,c,e) $F_h^{-1} = 1$, (b,d,f) $F_h^{-1} = 5$. The colour shows the enstrophy ratio ϕ.

The mode structures of the centrifugal instability for weak stratification shown in figure 15(c,d) are similar to those obtained by Sipp *et al.* (1999) in the absence of stratification. The elliptic-instability mode shown in figure 15(a,b) is also similar to that of Sipp *et al.* (1999), although the disturbance has wider distribution in our case; we must also take into account that the mode of Sipp *et al.* (1999) is shown by energy. The hyperbolic instabilities were not identified as a mode by Sipp *et al.* (1999); we will confirm the origin of the instabilities including the hyperbolic instabilities in the next subsection.

5.3. *Comparison between local and modal stability analysis*

In this subsection, we compare the local stability results and the modal stability results. Direct correspondence between the local and modal stability analysis would give a firm physical origin of the unstable modes found in the modal stability analysis because the mechanism of the instability is clear in the local stability analysis. Conversely, it further supports the usefulness of the local stability analysis.

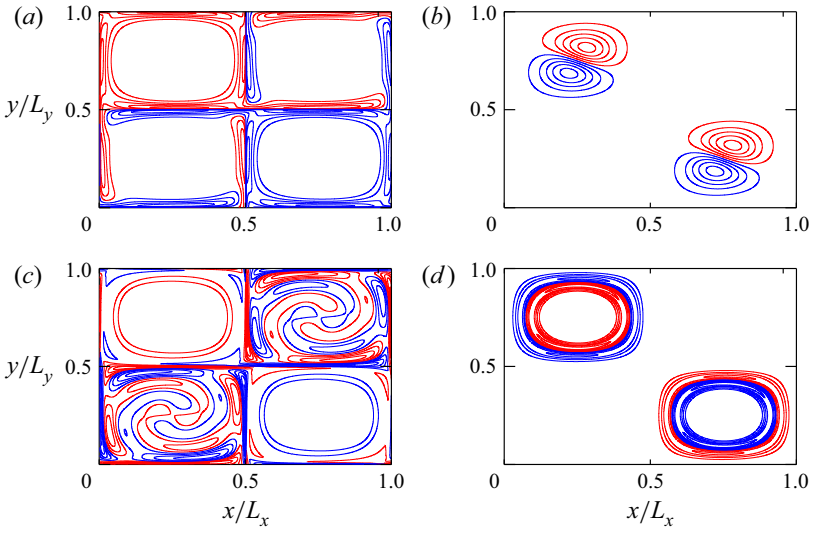

Figure 15. Mode structures shown by contours of ω_z' on the xy plane. Two-dimensional Taylor–Green vortices with $\varepsilon_e/\omega_{max} = 0.2$, $F_h^{-1} = 1$. All modes are anti-symmetric modes. (a) Pure-hyperbolic-instability mode with $|Ro^{-1}| = 2$, $k_zL_0 = 62.8$, $\sigma = 1.42$ and $\phi = 0.441$; (b) elliptic-instability mode with $|Ro^{-1}| = 2$, $k_zL_0 = 13.8$, $\sigma = 0.867$ and $\phi = 0$; (c) rotational-hyperbolic-instability mode with $|Ro^{-1}| = 3$, $k_zL_0 = 25.1$, $\sigma = 0.576$ and $\phi = 0.896$; (d) centrifugal-instability mode with $|Ro^{-1}| = 4$, $k_zL_0 = 62.8$, $\sigma = 0.394$ and $\phi = 0$. The contours of ω_z' are drawn as in figure 10.

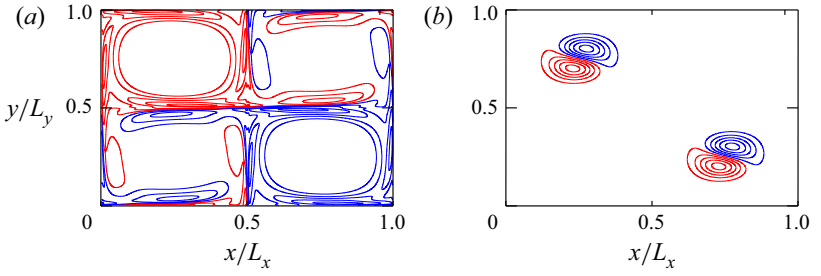

Figure 16. Mode structures shown by contours of ω_z' on the xy plane. Two-dimensional Taylor–Green vortices with $\varepsilon_e/\omega_{max} = 0.2$, $F_h^{-1} = 5$. All modes are anti-symmetric modes. (a) Pure-hyperbolic-instability mode with $|Ro^{-1}| = 2$, $k_zL_0 = 62.8$, $\sigma = 1.11$ and $\phi = 0.572$; (b) elliptic-instability mode with $|Ro^{-1}| = 3$, $k_zL_0 = 62.8$, $\sigma = 1.01$ and $\phi = 0$. The contours of ω_z' are drawn as in figure 10.

Figure 17 compares the structures of unstable modes to the corresponding solutions to the local stability equations for four cases: the rotational-hyperbolic-instability mode for $(F_h^{-1}, Ro^{-1}) = (0, 4)$ shown in figure 11(a), the centrifugal-instability mode for $(F_h^{-1}, Ro^{-1}) = (0, -4)$ shown in figure 11(b), the pure-hyperbolic-instability mode for $(F_h^{-1}, Ro^{-1}) = (5, 1)$ shown in figure 13(b) and the elliptic-instability mode for $(F_h^{-1}, Ro^{-1}) = (5, -3)$ shown in figure 16(b). The strato-hyperbolic instability is omitted because it has been already investigated by Suzuki *et al.* (2018) and Hattori *et al.* (2021). The horizontal divergence $\nabla_h \cdot \boldsymbol{u}_h' = \partial u'/\partial x + \partial v'/\partial y$, the vertical component of vorticity ω_z' and the density ρ' of the unstable mode on a streamline of nearly largest amplitude of ω_z' are plotted against time of fluid particle motion which is dictated by (2.15) (figure 17a,c,e,g); the corresponding variables p, q and s defined by (2.19a–c)

of the solution to the local stability equations on the same streamline are shown in figure 17(*b*,*d*,*f*,*h*), where the values are multiplied by $e^{-\sigma t}$ to compensate the exponential growth. The values are normalized by the maximum values to resolve arbitrariness of the initial amplitudes in the linear stability analysis. We observe good agreement between the modal and local results; there are some differences in amplitude ratios, but the shapes of the curves are in excellent agreement. Differences between the instabilities are also elucidated; the change in phase is 4π for the rotational-hyperbolic and the pure-hyperbolic-instability modes and 2π for the elliptic-instability mode, while the variables do not change their signs for the centrifugal-instability mode. These results establish the correspondence between local and modal stability results, clarifying the physical origin of each instability.

Figure 18 compares the growth rates obtained by the local and modal stability analysis; the growth rate $\sigma_{max}(Ro, F_h)$ obtained by local stability analysis is shown by lines as a function of Ro^{-1} for each instability, while the maximum growth rate obtained by modal stability analysis is shown for selected values of Ro^{-1} by solid circles. For the latter, the corrected growth rate in the absence of viscous effects was also estimated by subtracting the viscous contribution as

$$\sigma_{inv} = \sigma - \frac{1}{Re}\frac{\int \boldsymbol{u}' \cdot \nabla^2 \boldsymbol{u}' \,\mathrm{d}x\,\mathrm{d}y\,\mathrm{d}z}{\int |\boldsymbol{u}'|^2 \,\mathrm{d}x\,\mathrm{d}y\,\mathrm{d}z} \tag{5.12}$$

and is included as open circles; it should be noted that this does not coincide with the inviscid limit since the mode structures and the wavenumber are affected by viscous effects. The modal stability growth rates are smaller than $\sigma_{max}(Ro, F_h)$ except for the special case of the pure hyperbolic instability at $Ro^{-1} = 0$; this is reasonable since the modal stability growth rate cannot exceed the local stability results. The ratio of the growth rate is between 57 % and 99 % for weak stratification (figure 18*a*,*b*), while it drops to 24 % $\sim$ 68 % for the pure hyperbolic and centrifugal instabilities for strong stratification (figure 18*c*,*d*). The corrected growth rate of the elliptic instability is close to the local stability results. For the centrifugal instability, the corrected growth rate is close to the local stability results for weak stratification; however, the differences are remarkable for strong stratification. As shown by Yim & Billant (2016), the growth rate of the centrifugal instability is damped by viscous effects even at high Reynolds numbers for strong stratification since the wavenumber giving the maximum growth rate scales as $k \propto (Re/F_h)^{1/3}$ and is large. The differences would decrease for much higher Reynolds numbers and a wider range of wavenumbers; this may also be the case for the hyperbolic instabilities, although higher resolution is required to confirm it numerically.

6. Concluding remarks

The linear stability of an array of vortices in rotating stratified fluids has been studied by local and modal stability analysis. The 2-D Taylor–Green vortices are chosen as a base flow. The growth rate and the conditions of each instability are first estimated in the short-wave limit. Next, they are investigated numerically by local stability analysis and modal stability analysis. Several types of instability are identified: the pure hyperbolic instability, the strato-hyperbolic instability, the rotational-hyperbolic instability, the centrifugal instability and the elliptic instability; there are also a few instabilities which consist of two of the above instabilities (mixed hyperbolic instability in figure 9*a*,*b* and the mixed instability of the pure hyperbolic and strato-hyperbolic instabilities in figure 12*a*,*b*). The zigzag and radiative instability were not found in the present work. The zigzag instability has been found for a vortex pair; it may be absent for the 2-D

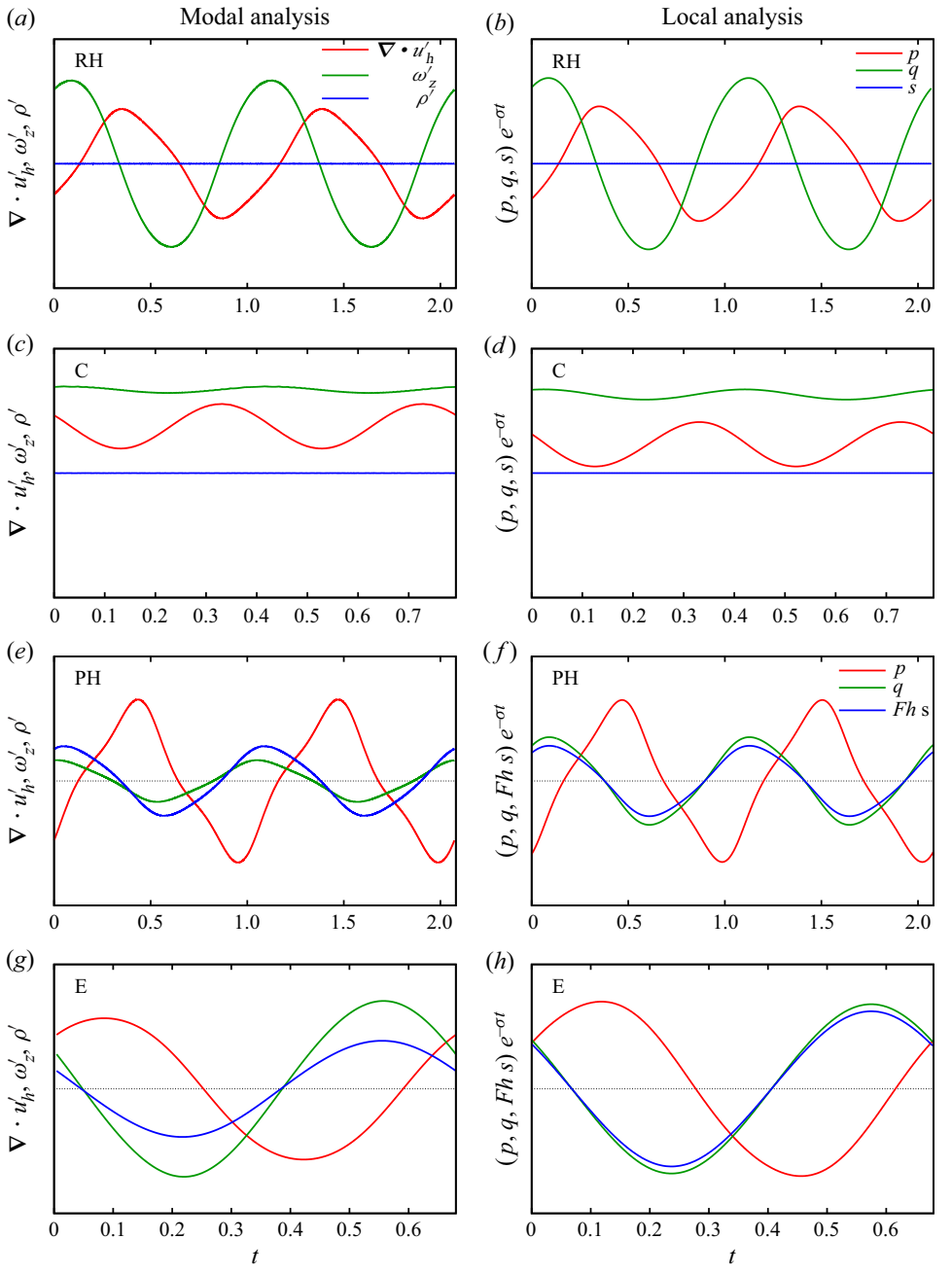

Figure 17. Comparison between modal and local stability analysis. (*a*,*c*,*e*,*g*) Values of $\nabla_h \cdot \boldsymbol{u}_h' = \partial u'/\partial x + \partial v'/\partial y$, ω_z' and ρ' of the unstable eigenmode obtained by modal stability analysis are shown as a function of time of a fluid particle on the streamline where ω_z' is maximum. (*b*,*d*,*f*,*h*) Corresponding values of p, q and s on the same streamline are multiplied by $\mathrm{e}^{-\sigma t}$ to compensate the exponential growth. (*a*,*b*) Rotational-hyperbolic-instability mode with $\varepsilon_e/\omega_{max} = 0$, $F_h^{-1} = 0$, $Ro^{-1} = 4$, $k_z L_0 = 25.1$, $\sigma = 0.729$ and $\beta = 0.9$; (*c*,*d*) centrifugal-instability mode with $\varepsilon_e/\omega_{max} = 0$, $F_h^{-1} = 0$, $Ro^{-1} = -4$, $k_z L_0 = 62.8$, $\sigma = 0.626$ and $\beta = 0.775$; (*e*,*f*) pure-hyperbolic-instability mode with $\varepsilon_e/\omega_{max} = 0$, $F_h^{-1} = 5$, $Ro^{-1} = 1$, $k_z L_0 = 62.8$, $\sigma = 1.44$ and $\beta = 0.9$; (*g*,*h*) elliptic-instability mode with $\varepsilon_e/\omega_{max} = 0.2$, $F_h^{-1} = 5$, $Ro^{-1} = -3$, $k_z L_0 = 62.8$, $\sigma = 1.01$ and $\beta = 0.225$.

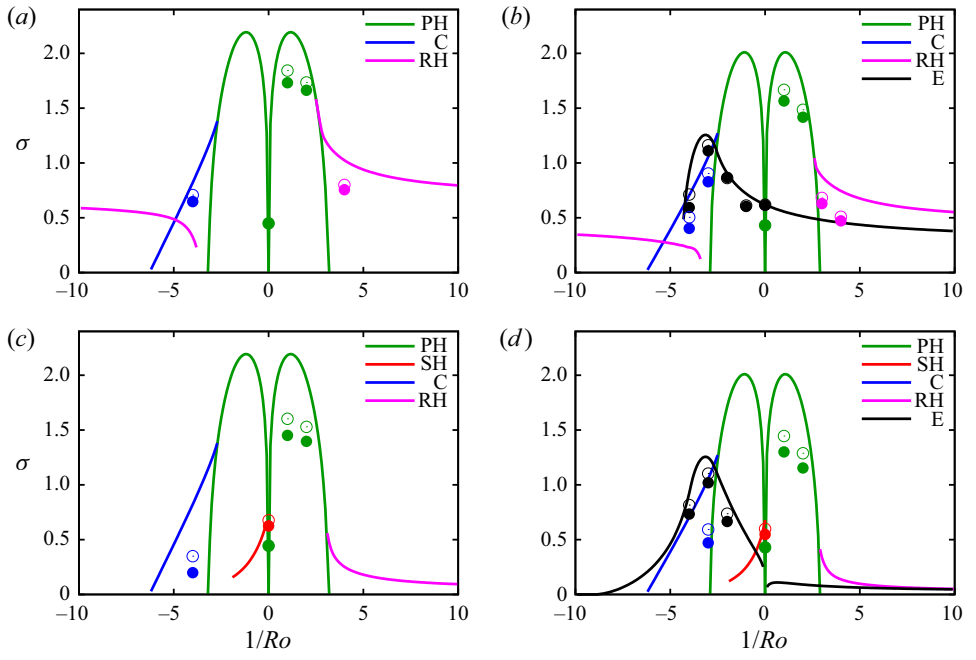

Figure 18. Growth rate $\sigma_{max}(Ro, F_h)$ as a function of Ro. Comparison between local stability analysis (lines) and modal stability analysis (solid circles); the growth rate for the inviscid case is also estimated by subtracting the viscous contribution for the modal stability analysis (open circles). (*a*) $\varepsilon_e/\omega_{max} = 0$, $F_h^{-1} = 0$; (*b*) $\varepsilon_e/\omega_{max} = 0.2$, $F_h^{-1} = 1$; (*c*) $\varepsilon_e/\omega_{max} = 0$, $F_h^{-1} = 5$; (*d*) $\varepsilon_e/\omega_{max} = 0.2$, $F_h^{-1} = 5$.

Taylor–Green vortices because of strong symmetry imposed by double periodicity. It may not be easy to find the radiative instability in the present case because it is not a strong instability (Park & Billant 2013). The characteristics of the instabilities and the effects of stratification and rotation are investigated in detail. In the absence of stratification, the pure hyperbolic instability is dominant when rotation is weak, although it vanishes in the non-rotating case; it is stabilized for strong rotation. For strong anti-cyclonic rotation, the elliptic instability or the centrifugal instability becomes dominant depending on the parameter values; further stronger rotation stabilizes both instabilities. For strong cyclonic rotation, the rotational-hyperbolic instability or the elliptic instability becomes dominant, although the growth rate of the latter is smaller than the anti-cyclonic case. When stratification is present, the strato-hyperbolic instability occurs for weak rotation. The rotational-hyperbolic instability and the elliptic instability under cyclonic rotation are weakened by stratification. The pure hyperbolic instability and the centrifugal instability are less affected by stratification, while the mode structures are flattened. Stratification also changes the instability condition of the elliptic instability under anti-cyclonic rotation; although it almost reverses the instability condition at $F_h^{-1} = \omega_{max}/2$, it has been found that the unstable region extends to $Ro^{-1} \approx 0$ near $\theta_0 = 0^\circ$ in the local stability analysis.

We emphasize that the whole picture of the instability of an array of vortices in rotating stratified fluids has been elucidated. The instability condition and the growth rate depend on the rotation of the system, the magnitude of stratification and the vorticity distribution. The important parameters of the vorticity distribution are the strain rates at the hyperbolic and elliptic stagnation points and the maximum vorticity. The estimates based on the local stability analysis summarized in table 1 are not only in good agreement with the

local stability results but also consistent with the modal stability results, whereas some differences remain at a finite Reynolds number as high as $Re = 10^5$. They would serve as useful sources of information for the instability of vortices in rotating stratified fluids in general and should be valuable for understanding their dynamics.

Another important contribution of the present work is the discovery of the rotational-hyperbolic-instability modes. Although the rotational-hyperbolic instability appeared in the investigation of Sipp *et al.* (1999) without much attention and was studied by Godeferd *et al.* (2001) by local stability analysis, the actual mode has been found for the first time in the present work to the best of the authors' knowledge. In addition, it has been further shown that the local stability analysis not only serves as a powerful tool for parametric study but also provides physical insight into the instabilities. Introduction of the realizability $\mathcal{R}$ proved helpful for interpreting the modal stability results at finite Reynolds numbers based on the local stability results.

Some future works are listed below. The effects of rotation and stratification on other flows possessing hyperbolic stagnation points, which include the Stuart vortices, vortex pairs and wake vortices such as the von Kármán vortex street, are of interest. How each instability evolves in the nonlinear regime is also of great interest. Some of them can destroy vortices, while some can promote merging of vortices or creation of strong vorticity (Hattori 2016, 2018), which will be studied by direct numerical simulation. In reality, the effects of non-uniform stratification and those of variation of the Coriolis parameter (β-effect) would be important; in-plane stratification would also be of great interest, although the base flow should be carefully chosen. They will be also investigated as future works.

Funding. This work was supported by JSPS KAKENHI 17K05561. Numerical calculations were performed on AFI-NITY at the Institute of Fluid Science, Tohoku University.

Declaration of interests. The authors report no conflict of interest.

Author ORCIDs.
Yuji Hattori https://orcid.org/0000-0002-1601-6416.

References

Arratia, C., Caulfield, C.P. & Chomaz, J.-M. 2013 Transient perturbation growth in time-dependent mixing layers. *J. Fluid Mech.* **717**, 90–133.

Aspden, J.M. & Vanneste, J. 2009 Elliptical instability of a rapidly rotating, strongly stratified fluid. *Phys. Fluids* **21**, 074104.

Bayly, B.J. 1988 Three-dimensional centrifugal-type instabilities in inviscid two-dimensional flows. *Phys. Fluids* **31**, 56–64.

Bayly, B.J., Holm, D.D. & Lifschitz, A. 1996 Three-dimensional stability of elliptical vortex columns in external strain flows. *Phil. Trans. R. Soc. Lond.* A **354**, 895–926.

Billant, P. 2000 Zigzag instability of vortex pairs in stratified and rotating fluids. Part 1. General stability equations. *J. Fluid Mech.* **660**, 354–395.

Billant, P. & Chomaz, J.-M. 2000*a* Experimental evidence for a new instability of a vertical columnar vortex pair in a strongly stratified fluid. *J. Fluid Mech.* **418**, 167–188.

Billant, P. & Chomaz, J.-M. 2000*b* Theoretical analysis of the zigzag instability of a vertical columnar vortex pair in a strongly stratified fluid. *J. Fluid Mech.* **419**, 29–63.

Billant, P. & Chomaz, J.-M. 2000*c* Three-dimensional stability of a vertical columnar vortex pair in a stratified fluid. *J. Fluid Mech.* **419**, 65–91.

Billant, P. & Chomaz, J.-M. 2001 Self-similarity of strongly stratified inviscid flows. *Phys. Fluids* **13**, 1645–1651.

Billant, P., Deloncle, A., Chomaz, J.-M. & Otheguy, P. 2010 Zigzag instability of vortex pairs in stratified and rotating fluids. Part 2. Analytical and numerical analyses. *J. Fluid Mech.* **660**, 396–429.

DELONCLE, A., BILLANT, P. & CHOMAZ, J.-M. 2008 Nonlinear evolution of the zigzag instability in stratified fluids: a shortcut on the route to dissipation. *J. Fluid Mech.* **599**, 229–239.
DELONCLE, A., BILLANT, P. & CHOMAZ, J.-M. 2011 Three-dimensional stability of vortex arrays in a stratified and rotating fluid. *J. Fluid Mech.* **678**, 482–510.
DONNADIEU, C., ORTIZ, S., CHOMAZ, J.-M. & BILLANT, P. 2009 Three-dimensional instabilities and transient growth of a counter-rotating vortex pair. *Phys. Fluids* **21**, 094102.
EDWARDS, W.S., TUCKERMAN, L.S., FRIESNER, R.A. & SORENSEN, D.C. 1994 Krylov methods for the incompressible Navier–Stokes equations. *J. Comput. Phys.* **110**, 82–102.
ETLING, D. 1989 On atmospheric vortex streets in the wake of large islands. *Meteorol. Atmos. Phys.* **41**, 157–164.
FRIEDLANDER, S. & VISHIK, M.M. 1991 Instability criteria for the flow of an inviscid incompressible fluid. *Phys. Rev. Lett.* **66**, 2204–2206.
GAU, T. & HATTORI, Y. 2014 Modal and non-modal stability of two-dimensional Taylor–Green vortices. *Fluid Dyn. Res.* **46**, 031410.
GODEFERD, F.S., CAMBON, C. & LEBLANC, S. 2001 Zonal approach to centrifugal, elliptic and hyperbolic instabilities in Stuart vortices with external rotation. *J. Fluid Mech.* **449**, 1–37.
GUIMBARD, D., LE DIZÈS, S., LE BARS, M., LE GAL, P. & LEBLANC, S. 2010 Elliptic instability of a stratified fluid in a rotating cylinder. *J. Fluid Mech.* **660**, 240–257.
HATTORI, Y. 2016 Concentration of vorticity in a destabilized vortex due to selective decay. *J. Fluid Mech.* **797**, 630–643.
HATTORI, Y. 2018 Concentration of vorticity due to selective decay in doubly periodic vortices and a vortex pair. *Fluid Dyn. Res.* **50**, 011405.
HATTORI, Y., SUZUKI, S., HIROTA, M. & KHANDELWAL, M. 2021 Modal stability analysis of arrays of stably stratified vortices. *J. Fluid Mech.* **909**, A4.
JULIEN, S., ORTIZ, S. & CHOMAZ, J.-M. 2004 Secondary instability mechanisms in the wake of a flat plate. *Eur. J. Mech. B/Fluids* **23**, 157–165.
KERSWELL, R.R. 2002 Elliptical instability. *Annu. Rev. Fluid Mech.* **34**, 83–113.
KLOOSTERZIEL, R.C. & VAN HEIJST, G.J.F. 1991 An experimental study of unstable barotropic vortices in a rotating fluid. *J. Fluid Mech.* **223**, 1–24.
LE DIZÈS, S. 2008 Inviscid waves on a Lamb–Oseen vortex in a rotating stratified fluid: consequences for the elliptic instability. *J. Fluid Mech.* **597**, 283–303.
LE DIZÈS, S. & BILLANT, P. 2009 Radiative instability in stratified vortices. *Phys. Fluids* **21**, 096602.
LEBLANC, S. 1997 Stability of stagnation points in rotating flows. *Phys. Fluids* **9**, 3566–3569.
LEBLANC, S. 2003 Internal wave resonances in strain flows. *J. Fluid Mech.* **477**, 259–283.
LEBLANC, S. & CAMBON, C. 1998 Effects of the Coriolis force on the stability of Stuart vortices. *J. Fluid Mech.* **356**, 353–379.
LEBLANC, S. & GODEFERD, F.S. 1999 An illustration of the link between ribs and hyperbolic instability. *Phys. Fluids* **11**, 497–499.
LEWEKE, T. & WILLIAMSON, C.H.K. 1998 Three-dimensional instabilities in wake transition. *Eur. J. Mech. B/Fluids* **17**, 571–586.
LIFSCHITZ, A. & HAMEIRI, E. 1991 Local stability conditions in fluid dynamics. *Phys. Fluids* A **3**, 2644–2651.
MIYAZAKI, T. 1993 Elliptical instability in a stably stratified rotating fluid. *Phys. Fluids* A **5**, 2702–2709.
MIYAZAKI, T. & ADACHI, K. 1998 Short-wavelength instabilities of waves in rotating stratified fluids. *Phys. Fluids* **10**, 3168–3177.
MIYAZAKI, T. & FUKUMOTO, Y. 1992 Three-dimensional instability of strained vortices in a stably stratified flow. *Phys. Fluids* A **4**, 2515–2522.
OTHEGUY, P., BILLANT, P. & CHOMAZ, J.-M. 2006*a* Elliptic and zigzag instabilities on co-rotating vertical vortices in a stratified fluid. *J. Fluid Mech.* **553**, 253–272.
OTHEGUY, P., BILLANT, P. & CHOMAZ, J.-M. 2006*b* The effect of planetary rotation on the zigzag instability of co-rotating vortices in a stratified fluid. *J. Fluid Mech.* **553**, 273–281.
PARK, J. & BILLANT, P. 2013 Instabilities and waves on a columnar vortex in a strongly stratified and rotating fluid. *Phys. Fluids* **25**, 086601.
PEYRET, R. 2010 *Spectral Methods for Incompressible Viscous Flow*. Springer.
POTYLITSIN, P.G. & PELTIER, W.R. 1998 Stratification effects on the stability of columnar vortices on the f-plane. *J. Fluid Mech.* **355**, 45–79.
POTYLITSIN, P.G. & PELTIER, W.R. 1999 Three-dimensional destabilization of Stuart vortices: the influence of rotation and ellipticity. *J. Fluid Mech.* **387**, 205–226.

PRALITS, J.O., GIANNETTI, F. & BRANDT, L. 2013 Three-dimensional instability of the flow around a rotating circular cylinder. *J. Fluid Mech.* **730**, 5–18.

RAYLEIGH, LORD 1917 On the dynamics of revolving fluids. *Proc. R. Soc. Lond.* A **93**, 148–154.

SINGH, S. & MATHUR, M. 2019 Effects of Schmidt number on the short-wavelength instabilities in stratified vortices. *J. Fluid Mech.* **867**, 765–803.

SIPP, D. & JACQUIN, L. 1998 Elliptic instability in two-dimensional flattened Taylor–Green vortices. *Phys. Fluids* **10**, 839–849.

SIPP, D., LAUGA, E. & JACQUIN, L. 1999 Vortices in rotating systems: centrifugal, elliptic and hyperbolic type instabilities. *Phys. Fluids* **11**, 3716–3728.

STEGNER, A., PICHON, T. & BEUNIER, M. 2005 Elliptical-inertial instability of rotating Kármán vortex streets. *Phys. Fluids* **17**, 066602.

SUZUKI, S., HIROTA, M. & HATTORI, Y. 2018 Strato-hyperbolic instability: a new mechanism of instability in stably stratified vortices. *J. Fluid Mech.* **854**, 293–323.

THORPE, S.A. 2005 *The Turbulent Ocean*, chap. 13. Cambridge University Press.

WAITE, M.L. & SMOLARKIEWICZ, P.K. 2008 Instability and breakdown of a vertical vortex pair in a strongly stratified fluid. *J. Fluid Mech.* **606**, 239–273.

YIM, E. & BILLANT, P. 2016 Analogies and differences between the stability of an isolated pancake vortex and a columnar vortex in stratified fluid. *J. Fluid Mech.* **796**, 732–766.

YOUSSEF, A. & MARCUS, P.S. 2003 The dynamics of jovian white ovals from formation to merger. *Icarus* **162**, 74–93.